

SRI International

AD-A277 028



Quarterly Technical Report 6•February 1994

IR MATERIALS PRODUCIBILITY

A. Sher, Program Director
M.A. Berding, Sr. Research Physicist
A.T. Paxton, Research Physicist
Physical Electronics Laboratory
M.W. Muller, Consultant

SRI Project 3820

Prepared for:

Contracting Officers Technical Representative
Defense Advanced Research Projects Agency
Microelectronics Technology Office (MTO)
3701 N. Fairfax Drive
Arlington, VA 22203-1714

Attn: Mr. Raymond Balcerak

ARPA Order No. 8557; Program Code Nos. 2H20, 2D10

Contract MDA972-92-C-0053

Covering the period: 1 November 1993 through 31 January 1994

The views and conclusions contained in this document are those of the authors and should not be interpreted as representing the official policies, either expressed or implied, of the Advanced Research Projects Agency or the U.S. Government.

APPROVED FOR PUBLIC RELEASE
DISTRIBUTION UNLIMITED

DTIC
ELECTE
MAR 16 1994
S B D

94-08459



94 3 15 051

IR MATERIALS PRODUCIBILITY

A. Sher, Program Director
M.A. Berding, Sr. Research Physicist
A.T. Paxton, Research Physicist
Physical Electronics Laboratory
M.W. Muller, Consultant

SRI Project 3820

Prepared for:

Contracting Officers Technical Representative
Defense Advanced Research Projects Agency
Microelectronics Technology Office (MTO)
3701 N. Fairfax Drive
Arlington, VA 22203-1714
Attn: Mr. Raymond Balcerak

ARPA Order No. 8557; Program Code Nos. 2H20, 2D10

Contract MDA972-92-C-0053

Covering the period: 1 November 1993 through 31 January 1994

The views and conclusions contained in this document are those of the authors and should not be interpreted as representing the official policies, either expressed or implied, of the Advanced Research Projects Agency or the U.S. Government.

APPROVED FOR PUBLIC RELEASE
DISTRIBUTION UNLIMITED

Approved:

Eric Pearson, Director
Physical Electronics Laboratory

Donald L. Nielson, Vice President
Computing and Engineering Sciences Division

REPORT DOCUMENTATION PAGE			Form Approved OMB No. 0704-0188	
Public reporting burden for this collection of information is estimated to average 1 hour per response, including the time for reviewing instructions, searching existing data sources, gathering and maintaining the data needed, and completing and reviewing the collection of information. Send comments regarding this burden estimate or any other aspect of this collection of information, including suggestions for reducing this burden, to Washington Headquarters Services, Directorate for Information Operations and Reports, 1215 Jefferson Davis Highway, Suite 1204, Arlington, VA 22202-4302, and to the Office of Management and Budget, Paperwork Reduction Project (0704-0188), Washington, DC 20503.				
1. AGENCY USE ONLY (Leave Blank)		2. REPORT DATE February 1994	3. REPORT TYPE AND DATES COVERED Quarterly Tech. Rpt. 6, 11-1-93 to 1-31-94	
4. TITLE AND SUBTITLE IR Materials Producibility			5. FUNDING NUMBERS	
6. AUTHORS A. Sher, M.A. Berding, A.T. Paxton, SRI International M. Muller, Consultant				
7. PERFORMING ORGANIZATION NAME(S) AND ADDRESS(ES) SRI International 333 Ravenswood Avenue Menlo Park, CA 94025-3493			8. PERFORMING ORGANIZATION REPORT NUMBER	
9. SPONSORING/MONITORING AGENCY NAME(S) AND ADDRESS(ES) Advanced Research Projects Agency Microelectronics Technology Office (MTO) Infrared Focal Plane Array Program 3701 N. Fairfax Drive Arlington, VA 22203-1714			10. SPONSORING/MONITORING AGENCY REPORT NUMBER	
11. SUPPLEMENTARY NOTES				
12a. DISTRIBUTION/AVAILABILITY STATEMENT Approved for public release; distribution unlimited			12b. DISTRIBUTION CODE	
13. ABSTRACT (Maximum 200 words) In this quarter we have completed an extensive paper on native point defects in $\text{Hg}_{0.8}\text{Cd}_{0.2}\text{Te}$, and submitted it to Physical Review B. We calculated the binding energy of a mercury vacancy tellurium antisite defect complex in $\text{Hg}_{0.8}\text{CdTe}$ and estimated the complex density and its consequences on materials processing. The defect formation energies in CdTe and ZnSe , including gradient corrections to the local density approximation, were calculated, and estimates of the neutral defect concentrations in ZnSe were made. We have continued to develop a method to calculate the defect ionization energies in CdTe , ZnSe , and LiNbO_3 . Preliminary prediction of the defect densities in $\chi = 0.17$ LWIR $\text{Hg}_{1-\chi}\text{Zn}_\chi\text{Te}$ were made and compared to results in HgCdTe . We continued to develop a method to calculate the temperature dependence of the semiconductor bandgaps. Modifications of our thermodynamical codes for the LiNbO_3 problem were made so that the stoichiometry and temperature may be specified and the defect densities determined.				
14. SUBJECT TERMS native point defect; defect density; photonic material; IRFPA; HgTe ; CdTe ; ZnSe ; HgCdTe ; LiNbO_3 .			15. NUMBER OF PAGES	
			16. PRICE CODE	
17. SECURITY CLASSIFICATION OF REPORT Unclassified	18. SECURITY CLASSIFICATION OF THIS PAGE Unclassified	19. SECURITY CLASSIFICATION OF ABSTRACT Unclassified	20. LIMITATION OF ABSTRACT Unlimited	

SUMMARY

The work summarized in this report covers the sixth quarter of a program with a goal that is threefold: first, to study the properties of native point defect in infrared focal-plan array (IRFPA) active and substrate materials; second, to study the properties of native point defects in two classes of photonic materials, the wide-gap II-VI compounds (ZnSe as the prototype for which impurity properties will also be calculated) and the nonlinear optical materials (LiNbO₃ as the prototype); and third to study the properties of HgZnTe as a VLWIR detector material. Our accomplishments in the sixth quarter include

- Completion of an extensive paper on native point defects in Hg_{0.8}Cd_{0.2}Te as a function of processing conditions for submission to Physical Review B.
- Calculation of the binding energy of a mercury vacancy tellurium anti-site defect complex in Hg_{0.8}Cd_{0.2}Te and estimates of the complex density and its consequences on materials processing and device performance.
- Completion of the defect formation energies in CdTe, including gradient corrections to the local density approximation.
- Completion of the defect formation energies in ZnSe, including gradient corrections to the local density approximation, and estimates of the neutral defect concentrations.
- Continued calculation of the defect ionization energies in CdTe, ZnSe, and LiNbO₃.
- Preliminary prediction of the defect densities in $x = 0.17$ LWIR Hg_{1-x}Zn_xTe.
- Continued development of a method to calculate the temperature dependence of the semiconductor bandgaps, with initial agreement at 300 K both for Hg_{0.78}Cd_{0.22}Te and GaAs.
- Modification of our thermodynamic codes for the LiNbO₃ problem so that the stoichiometry and temperature may be specified and the defect densities determined.

1	NATIVE POINT DEFECTS IN HgCdTe AND RELATED IR MATERIALS	1
1.1	NATIVE POINT DEFECTS IN Hg _{0.8} Cd _{0.2} Te	1
1.2	MERCURY VACANCY TELLURIUM ANTISITE COMPLEX	1
1.3	NATIVE POINT DEFECTS IN CdTe	2
1.4	TEMPERATURE-DEPENDENT BANDGAP	3
2	NATIVE POINT DEFECTS IN LWIR HgZnTe	4
3	WIDE-GAP II-VI COMPOUNDS (ZnSe AS PROTOTYPE)	6
4	NONLINEAR OPTICAL MATERIALS (LiNbO ₃ AS THE PROTOTYPE)	9
5	WORK PLANNED	9

APPENDIX A

APPENDIX B

Accession For	
NTIS GRA&I	<input checked="" type="checkbox"/>
DTIC TAB	<input type="checkbox"/>
Unannounced	<input type="checkbox"/>
Justification	
By	
Distribution	
Availability Codes	
Dist	Avail and/or Special
A-1	

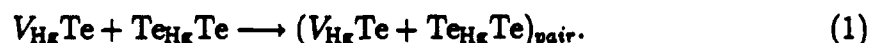
1. NATIVE POINT DEFECTS IN HgCdTe AND RELATED IR MATERIALS

1.1 NATIVE POINT DEFECTS IN $\text{Hg}_{0.8}\text{Cd}_{0.2}\text{Te}$

We have completed an extensive paper on the native point defects in $\text{Hg}_{0.8}\text{Cd}_{0.2}\text{Te}$; a copy of this paper is included as Appendix A.

1.2 MERCURY VACANCY TELLURIUM ANTISITE COMPLEX

We have completed a preliminary calculation of the mercury vacancy tellurium antisite electronic binding energy and find an energy of 1.1 eV per pair. This binding energy corresponds to the reaction



From the density of the isolated mercury vacancy, V_{Hg} , and tellurium antisites, Te_{Hg} , the density of the pair, $(V_{\text{Hg}}\text{Te} + \text{Te}_{\text{Hg}}\text{Te})_{\text{pair}}$, can be calculated via the mass action relation

$$\frac{[V_{\text{Hg}}\text{Te}][\text{Te}_{\text{Hg}}\text{Te}]}{[V_{\text{Hg}}\text{Te} + \text{Te}_{\text{Hg}}\text{Te}]_{\text{pair}}} = K_{\text{pair}}. \quad (2)$$

If we assume that the defect formation free energy from changes to the vibrational spectrum are similar for the isolated defects and the pair, we can calculate the reaction constant as

$$K_{\text{pair}} = 12[ls]^{-1} \exp\left(\frac{1.1\text{eV}}{k_B T}\right) \quad (3)$$

where $[ls]$ is the density of lattice sites. The factor of 12 is the number of second nearest neighbor sites (but first nearest cation neighbor sites) and accounts for the degeneracy in the number of ways a pair can be formed in which one of the pairs occupies a particular lattice.

Applying the reaction constant, we have calculated the number of pairs present in material equilibrated at 500°C for the mercury-rich and tellurium-rich conditions. Results are summarized in Table 1. We have also estimated the concentration of tellurium antisites present following a low-temperature (250°C) mercury-saturated anneal, assuming that the mercury vacancies can reach equilibrium, but that the tellurium antisites are frozen-in at their 500°C levels. The freezing-in of the antisites is proposed because of the slow diffusion rate expected for this defect at lower temperatures; in this example we have assumed that the tellurium antisite diffusion effectively stops at 500°C, and therefore the antisites are frozen in at their 500°C levels. In contrast, if the tellurium antisites are assumed to fully equilibrate at 250°C their concentrations would only be $\sim 6 \times 10^6 \text{ cm}^{-3}$. At this point we do not know at what temperature the tellurium antisite diffusion effectively stops; this will be determined by the concentration of the vacancy-antisite pairs if the antisite diffusion is via a vacancy mechanism. An estimate of the critical temperature at which the tellurium antisite diffusion ceases and the frozen-in tellurium antisite concentrations,

$[Te_{Hg}]$, will be made next quarter. If $[Te_{Hg}] \simeq 10^{14} - 10^{15} \text{ cm}^{-3}$, this will be an indication that the antisite is the residual donor and will allow us to develop strategies for reducing the residual donor density.

Table 1. Neutral defect concentrations including the mercury vacancy tellurium antisite pairs. For 500°C, full equilibrium is assumed achieved. For the 250°C mercury-saturated anneal, the total tellurium antisite concentrations are assumed frozen-in at their 500°C levels.

Annealing condition	$[V_{Hg}] (\text{cm}^{-3})$	$[Te_{Hg}] (\text{cm}^{-3})$	$[V_{Hg}Te_{Hg}]_{pairs} (\text{cm}^{-3})$
T=500°C; Te-saturated	9.62×10^{15}	2.20×10^{16}	2.58×10^{18}
T=500°C; Hg-saturated	1.37×10^{14}	4.50×10^{12}	7.52×10^{12}
T=250°C; Hg-saturated following a T=500°C; Te-saturated anneal	3.58×10^9	2.30×10^{16}	3.00×10^{17}
T=250°C; Hg-saturated following a T=500°C; Hg-saturated anneal	3.58×10^9	1.06×10^{13}	1.37×10^{12}

1.3 NATIVE POINT DEFECTS IN CdTe

We have completed the calculation of the electronic contribution to the native point defect formation energies in CdTe using the full-potential local-density approximation with the linearized muffin-tin orbital (LMTO) basis. Gradient corrections were also computed. These two contributions defect formation energies are listed in Table 2. These energies can be used to predict the neutral native defect concentrations; this calculation will be completed next quarter. The corresponding numbers for HgTe are listed in Table 3. One should not try to infer the primary defects from the defect formation energies alone, without considering the vibrational entropy and vapor phase chemical potential contribution to the defect formation free energies.

Table 2. Neutral native point defect formation energies in CdTe. LDA is the contribution from the local-density calculation and GC is the correction from the gradient correction energy.

Defect	Defect reaction	LDA	GC	Total
V_{Cd}	$CdTe \rightarrow V_{Cd}Te + Cd_{free}$	4.152	-0.463	3.689
V_{Te}	$Cd_{free} \rightarrow CdV_{Te}$	0.870	+0.315	1.185
Cd_{Te}	$2Cd_{free} \rightarrow CdCd_{Te}$	-1.212	+1.091	-0.121
Te_{Cd}	$2CdTe \rightarrow Te_{Cd}Te + 2Cd_{free}$	7.062	-1.150	5.912
$Cd_{I_{Cd}}$	$Cd_{free} \rightarrow Cd_{I_{Cd}}$	0.384	0.450	0.834
$Cd_{I_{Te}}$	$Cd_{free} \rightarrow Cd_{I_{Te}}$	5.424	-0.698	4.726
$Te_{I_{Cd}}$	$CdTe \rightarrow Te_{I_{Cd}} + Cd_{free}$	0.546	0.391	0.937

1.4 TEMPERATURE-DEPENDENT BANDGAP

When the temperature of the lattice is increased, the lattice expands. This expansion, usually called dilation, decreases the bandgap. The number of phonons in the lattice increases with temperature. The change in potentials caused by the displacement of atoms from their equilibrium positions introduces an electron phonon interaction. These interactions, viewed as a perturbation, will change the electronic states, that is, the band structure. A major contribution to the bandgap change with temperature arises from this interaction.

The electron acoustic phonon interactions are usually parameterized in terms of wave-vector- and energy-independent deformation potential coupling constants. These constants are extracted from hydrostatic experiments that measure the change of symmetry point energies with pressure. In addition, only a few phonons, such as Γ , X, or L, are used; the measured atomic displacements due to other phonons are virtually unknown. Although these calculations based on this procedure yield correct trends in large-gap materials, the uncertainty in measured values, and hence the input parameters, yields ambiguous results for small-gap semiconductors.

Our calculations generalized the above approach considerably. We use accurate tight-binding band structures in the calculation of the dynamical matrix and electron-phonon interaction. In addition, we include contributions from all six phonon modes, with wave vectors spanning the entire Brillouin Zone.

These calculations require knowledge of spatial dependence of atomic potentials in the bulk. We assume that attractive interatomic matrix elements vary as r^m and the Coulomb repulsive interaction varies as V_0/r^{2m} . The two unknowns, m and V_0 , are adjusted so that total energy calculations yield an accurate equilibrium bond length and bulk modulus.

Once the spatial dependence of potentials is known, the dynamical matrix, which is the second derivative of the potential divided by the appropriate atomic mass, is

calculated and diagonalized to obtain the atomic displacements for a given phonon wave vector and branch.

Because the atomic displacements are small compared to the bond length, the change in potentials is obtained by a Taylor's expansion and only the first two terms are retained. The change in energy state at a given electron wave vector is obtained in a second-order, stationary-state perturbation theory. This procedure is usually called a rigid ion approximation.

Summarizing the steps involved in the calculations; (a) Choose the energy state whose temperature variation needs to be obtained. Get the corresponding electron wave vector, k . (b) Choose a phonon wave vector, q . (c) Calculate the dynamical matrix and diagonalize it to get the atomic displacements for all six modes, (d) From a knowledge of first and second derivatives of the potentials in the local basis, calculate the matrix elements, $\langle k|H_1|k \rangle$ and $|\langle k - q|H_2|k \rangle|^2$. (e) From the potential well expressions derived from second-order perturbation theory, the change in energy is obtained. The calculation of energy gap variation requires repeating the above procedure for conduction and valence band edge.

The calculations are carried for the $\text{Hg}_{0.78}\text{Cd}_{0.22}\text{Te}$ alloy.

The calculated change in the gap at 300 K is 95 meV, which is in excellent agreement with the experimental value of 98 meV. We are currently calculating the change for a larger temperature range in various semiconductors. The results will be provided in the next report.

2. NATIVE POINT DEFECTS IN LWIR HgZnTe

We have estimated the concentrations of native point defects in $x = 0.17 \text{ Hg}_{1-x}\text{Zn}_x\text{Te}$ based on our results in $x = 0.2 \text{ Hg}_{1-x}\text{Cd}_x\text{Te}$. Both materials consist mostly of HgTe , the primary difference being the difference in the lattice constants of the material. For HgCdTe (at any x) the lattice constant, a , is 6.454 Å, while for $x = 0.17 \text{ Hg}_{1-x}\text{Zn}_x\text{Te}$ $a = 6.378$; we have used an elastic continuum model to estimate the native defect formation energy change due to this difference in lattice constant. Results of this calculation are given in Table 3.

We have calculated the total (neutral plus ionized) native defect concentrations for LWIR HgCdTe and HgZnTe under mercury-saturated conditions and as a function of temperature; results are given in Figure 1. In this calculation we have assumed that the band structure and its temperature dependence are the same in HgZnTe and HgCdTe . While this is not likely to be rigorously true, the experimental data base for HgZnTe is far more limited and thus we are forced to make this approximation. Once we have completed our calculation of the temperature dependence of the bandgap, we will calculate the band structure properties for HgZnTe rather than borrow them from the HgCdTe experiments.

From Figure 1 we see that the mercury vacancy, tellurium antisite, and mercury interstitial densities in HgZnTe are all approximately a factor of two smaller than in HgCdTe . This difference is still subject to refinement and may increase. However

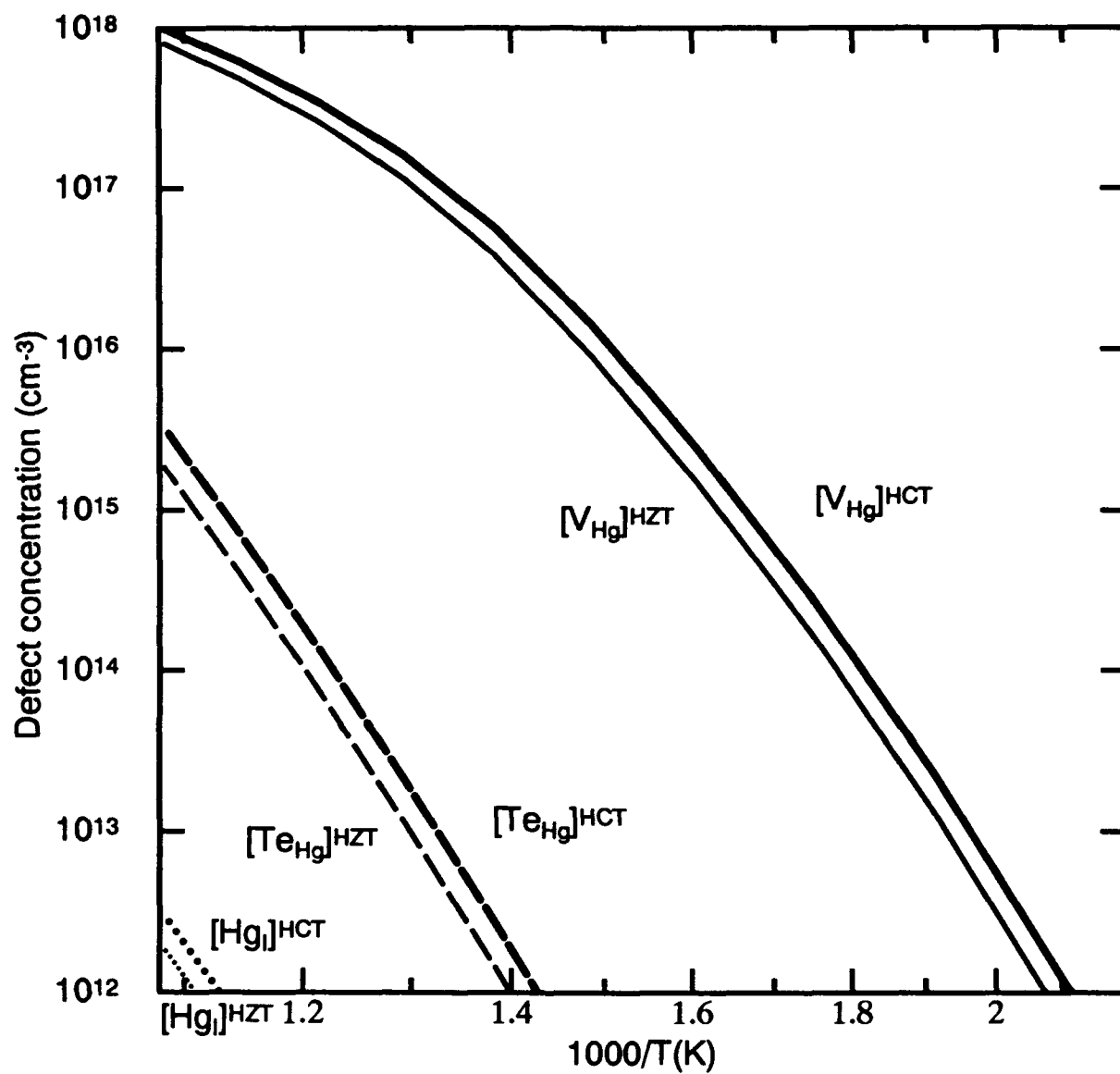


Figure 1. Defect concentrations in LWIR HgCdTe and HgZnTe under mercury-saturated conditions

at present predicted differences in mercury vacancy and mercury interstitial densities do not account for the experimentally observed difference in the mercury diffusion rates between the two materials and the superior bake stability of HgZnTe. We thus tentatively conclude that this difference in diffusion rates is not due to differences in the concentration of the diffusion species, but rather must be due to differences in the migration energy of the vacancies and interstitials in the two materials. Because the average lattice spacing in HgZnTe is smaller than that in HgCdTe, a smaller migration energy in HgCdTe is expected.

Table 3. Electronic contribution to the native defect formation energy in HgCdTe and $\text{Hg}_{0.17}\text{Zn}_{0.83}\text{Te}$.

Defect	HgCdTe	HgZnTe
V_{Hg}	2.09	2.14
V_{Te}	1.47	1.52
Te_{Hg}	0.46	0.53
Hg_{Te}	3.12	3.17
$\text{Hg}_{\text{I}_{\text{Hg}}}$	1.21	1.27
$\text{Hg}_{\text{I}_{\text{Te}}}$	1.12	1.16
$\text{Te}_{\text{I}_{\text{Hg}}}$	3.38	3.42
$\text{Te}_{\text{I}_{\text{Te}}}$	3.37	3.45

3. WIDE-GAP II-VI COMPOUNDS (ZnSe AS PROTOTYPE)

We have completed the calculation of the native point defect formation energies in ZnSe using the full-potential local-density approximation with the linearized muffin-tin orbital (LMTO) basis. Gradient corrections were also computed. Preliminary results using a small basis set size were given in Quarterly Technical Report 3. The calculations completed this quarter use a more converged basis set. The energies are summarized in Table 4. The defect formation energy and energy coming from the modifications in the vibrational modes of the system were reported in Quarterly Technical Report 3. Direct interpretation of the numbers appearing in Table 4 is difficult because these energies do not include the chemical potential of the free Zn atom, which can be substantial; this chemical potential is included in our quasichemical analysis of the defect concentrations.

Table 4. Neutral native point defect formation energies in ZnSe. LDA is the contribution from the local-density calculation and GC is the correction from the gradient correction energy.

Defect	Defect reaction	LDA	GC	Total
V_{Zn}	$ZnSe \longrightarrow V_{Zn}Se + Zn_{free}$	5.089	-0.460	4.629
V_{Se}	$Zn_{free} \longrightarrow ZnV_{Se}$	0.716	+0.322	1.038
Zn_{Se}	$2Zn_{free} \longrightarrow ZnZn_{Se}$	-1.373	+1.002	-0.371
Se_{Zn}	$2ZnSe \longrightarrow Se_{Zn}Se + 2Zn_{free}$	9.574	-1.158	8.416
$Zn_{I_{Zn}}$	$Zn_{free} \longrightarrow Zn_{I_{Zn}}$	1.103	+0.318	1.421
$Zn_{I_{Se}}$	$Zn_{free} \longrightarrow Zn_{I_{Se}}$	1.358	+0.258	1.616
$Se_{I_{Zn}}$	$ZnSe \longrightarrow Se_{I_{Zn}} + Zn_{free}$	7.545	-0.748	6.797
$Se_{I_{Se}}$	$ZnSe \longrightarrow Se_{I_{Se}} + Zn_{free}$	9.098	-0.854	8.244

In Figure 2 we show a plot of the neutral defect concentrations as a function of zinc pressure over the single phase stability region for material equilibrated at 600°C. The zinc vacancy, V_{Zn} , and the selenium antisite, Se_{Zn} , are the dominant defects, although even at this elevated temperature their concentrations are not comparable to desired dopant concentrations and therefore might be dismissed as potential compensating defects. Because we have not yet included the ionization states of these defects, this conclusion must be viewed as very tentative. We are currently working on this problem.

Although we have calculated the neutral native defect concentrations at 600°C, in fact we are interested in what happens in the material at the low temperatures used during molecular beam epitaxial (MBE) growth. While the calculation of the equilibrium defect densities at lower temperatures is straightforward, a number of complexities must be considered. First, the effective zinc and selenium pressure during the growth must be determined so that the chemical potential of these species in the solid can be specified. Second, there is a question about whether MBE growth constitutes an equilibrium, quasiequilibrium, or highly nonequilibrium process. Depending on which of these most closely describes the experimental conditions used, we can determine the applicability of an equilibrium or constrained quasiequilibrium quasichemical analysis to the problem. It is most likely that MBE growth of ZnSe constitutes a quasiequilibrium situation, in which case there are straightforward modifications to our present formalism that will permit us to calculate the defect concentrations under quasiequilibrium conditions. We have a theory of MBE growth of wide-gap semiconductors mostly cnonpleted. However, completing it and applying it to this problem is not possible at our current funding level. Therefore, to proceed for now, we will make an educated guess at what is happening on the growth surface. Finally, one must consider the mobility of the native defects in the MBE material during growth, both on the surface and in the bulk, to determine whether equilibrium

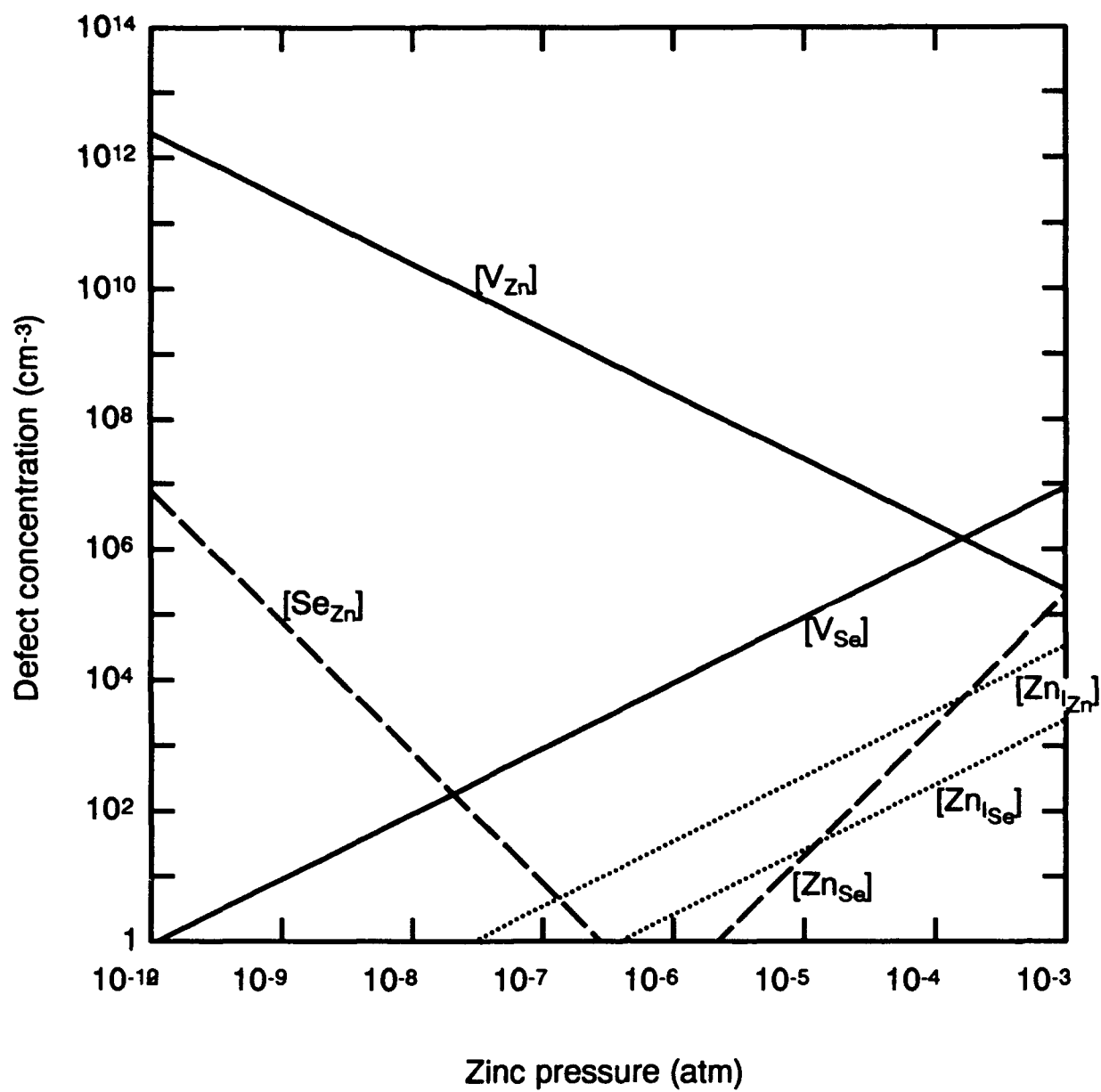


Figure 2. Neutral native defect concentrations
in ZnSe at 600° C

or quasiequilibrium can be reached. It is doubtful that defects such as the selenium antisite will equilibrate once they are locked into the bulk, because the diffusion of this defect is likely to be complex, involving one or more additional native defects. We are prepared to address these important issues in our future work.

This quarter we spoke with Dr. M. Haase at 3M Corporation and Dr. Diego Olego at Philips Laboratories about our work in ZnSe to explore areas in which our theory might be of assistance to their experimental program. A summary of this correspondence is included as Appendix B.

4. NONLINEAR OPTICAL MATERIALS (LiNbO₃ AS THE PROTOTYPE)

We have modified our quasichemical programs that predict the native defect concentrations in a binary or pseudobinary material as a function of the temperature and chemical potential, to allow the specification of the temperature and the material stoichiometry as the external parameters. This modification is necessary to calculate the defect concentrations in LiNbO₃, which, when grown congruently, is known to have a lithium-to-niobium ratio of 0.486:0.514. By specifying this stoichiometry in our mass action formalism, we can then predict the concentrations of the native defects. The complexity comes in first choosing the candidate defects that might account for the nonstoichiometry and secondly to calculate the formation energy of these defects. Several models of defects to account for the lithium-to-niobium ratio have been proposed in the literature, which we have discussed at some length in previous reports, and from which we have chosen several candidate native point defects for calculation of the native point defect densities. Several of the models involve extended defects such as stacking faults which will not be included in our analysis.

We are currently working on the determination of the ionization states of the native defects in LiNbO₃ so that we may predict the density of both neutral and ionized defects. Another ingredient necessary in the calculation of the ionized defect densities is the intrinsic reaction constant that depends on the band structure properties of the material. Unfortunately, for LiNbO₃ there is less experimental information available on the band structure properties than in the other systems we are studying and therefore we must rely on our own calculations of the electron and hole effective density of states for the determination of the intrinsic reaction constant. We have begun to extract these parameters this quarter. Once these native defect ionization energies and the intrinsic reaction constant are determined, we can then predict the native defect concentrations as a function of the lithium-to-niobium ratio.

5. WORK PLANNED

In the next quarter we will continue to study the mercury vacancy tellurium antisite defect complex in HgCdTe. Strategies for improving the calculation of the defect densities in HgZnTe will be investigated. We will continue our study of defects in CdTe, ZnSe, and LiNbO₃ this next quarter, focusing on the defect ionization energies.

Once the defect ionization energies are calculated in CdTe and ZnSe, the prediction of the defect densities will be straightforward. We will extract the band structure properties of LiNbO₃ for input into the defect density calculation. We will continue our work on the temperature dependence of the bandgap in the semiconductors.

APPENDIX A

**First-principles calculation of native point
defect densities in $\text{Hg}_{0.8}\text{Cd}_{0.2}\text{Te}$**

First-principles calculation of native defect densities in $\text{Hg}_{0.8}\text{Cd}_{0.2}\text{Te}$

M. A. Berding, M. van Schilfgaarde, and A. Sher
SRI International, Menlo Park, California 94025
(March 2, 1994)

We use a quasicchemical formalism to make quantitative predictions of the native point defect densities in $\text{Hg}_{0.8}\text{Cd}_{0.2}\text{Te}$. The electronic contribution to the defect formation free energy is calculated using the self-consistent first-principles full-potential linearised muffin-tin orbital method and the local-density approximation. A gradient correction is added to the LDA result so that absolute reference to the chemical potential of the mercury vapor phase can be made. A Green's function approach based on a valence force field plus a point Coulomb model is used to calculate the vibrational contributions to the defect free energy (both energy and entropy). We find the double acceptor mercury vacancy is the dominant defect, in agreement with previous interpretations of experiments. The tellurium antisite is also found to be an important defect in this material. Predictions of the low-temperature hole concentrations are made as a function of annealing temperature and compared with available experiments. The order of magnitude of our predictions agrees well with experimental results, and discrepancies can be attributed to contributions to the free energy that we have neglected or to inaccuracies in the intrinsic reaction constant used. Suggestions for further experimental work are made.

61:72.J, 61:72.C, 71:55.G, 42:70.K

I. INTRODUCTION

The pseudobinary semiconductor alloy $\text{Hg}_{1-x}\text{Cd}_x\text{Te}$ with $x=0.22$ is currently the material of choice for high-performance detectors in the long-wavelength infrared (8–14 μm). Unlike other II-VI systems, both extrinsic p- and n-type doping can be achieved in $\text{Hg}_{0.8}\text{Cd}_{0.2}\text{Te}$ although in as-grown material the electrical properties are often determined by native point defect concentrations. The dominant defect is believed to be a double-acceptor mercury vacancy¹; post-growth low-temperature mercury-saturated anneals are routine for the reduction of the mercury vacancy concentration. As in other semiconductors, it is more difficult to establish the presence and identity of neutral and compensating point defects, much less to determine their concentrations. Diffusion measurements² indicate the presence of mercury vacancies and mercury interstitials, as well as tellurium interstitials, although no unambiguous determination of their densities can be made from these experiments.

Although extended defects such as dislocations often appear to be the performance limiter in current state-of-the-art $\text{Hg}_{0.8}\text{Cd}_{0.2}\text{Te}$ devices,³⁻⁵ a number of mysteries still persist that may relate to native point defects. (1) For operation at 40 K, there is a variation in R_0A_j and lifetime among pixels with no etch pits,³ indicative of spatial nonuniformity in the material that is unrelated to dislocations. (2) An as yet unidentified donor limits the minimum n-type carrier concentrations obtainable during a mercury-saturated low-temperature anneal of the material. While the pressure and temperature dependence of this residual donor does not appear to correlate with the equilibrium dependencies of any native point defect,⁶ the nearly universal presence of the donor in liquid phase epitaxy (LPE), solid-state recrystallized (SSR), and molecular beam epitaxy (MBE) materials and its elusive nature do suggest that a native point defect is responsible. (3) Undoped LPE material that has been subjected to a low-temperature, mercury-saturated anneal and nominally converted to n-type shows an anomalously low mobility. One interpretation is that it is a consequence of interpenetrating p- and n-type regions, with the high effective-mass holes lowering the measured Hall mobilities.⁷ If this model proves to be correct, it may well be a native point defect that causes nonuniform annealing of the material. To overcome this low mobility, a donor impurity is added in concentrations above that of the unknown residual donor. Thus, to lower the n-doping to desirable levels, an understanding of the origin of the doping, and the low mobility and a recipe for its elimination are needed. (4) The identity of the primary Shockley-Reed-Hall (SRH) recombination centers has not been established; if they can be correlated with native point defects, strategies for their elimination can be developed. (5) MBE material is often n-type as grown⁸ and may be related to a nonequilibrium population of native point defects.

Unraveling the matrix of usually indirect and often contradictory experimental data on the native point defects in semiconductors is a complicated task, especially when the defects may be spatially varying. Numerous theoretical efforts have utilized first-principles methods to elucidate the properties of native point defects in the group IV, III-V, and II-VI semiconductors (see for example Refs. 9–12). While these studies have led to much insight into the properties of the point defects, no quantitative predictions of the defect densities were made. Several earlier theoretical studies

have looked at the properties of defects in HgCdTe^{13-16} although once again no quantitative predictions of defect densities were given.

Our goal in this paper is to theoretically identify the important native defects in HgCdTe , to calculate their densities as a function of growth and processing conditions, to substantiate the experimentally deduced properties of the native defects, and to begin to unravel the remaining mysteries in this material. To express the concentration of the native point defects in terms of their formation free energies, we employ the quasichemical formalism. In addition to the electron and hole, we have included eight native point defects (and their ionized species) in the analysis: the mercury and tellurium vacancies, the mercury and tellurium antisites, and two types of mercury and tellurium tetrahedral interstitials – one surrounded by four cation near-neighbors and one surrounded by four anion near-neighbors. As we will show, we have attempted to incorporate all of the important contributions to the free energy and adopt a first-principles approach for most of the quantities we calculate. The only significant empirical data we employ are those needed to obtain the temperature-dependent intrinsic reaction constant. Our calculated native defect concentrations are in quantitative agreement with the available experiment data. To our knowledge, this is the first attempt in any material to carry through a comprehensive theory of the native point defect concentrations essentially from first principles.¹⁷

A number of features make our study of defects in $\text{Hg}_{0.8}\text{Cd}_{0.2}\text{Te}$ unique, and permit us to calculate absolute defect concentrations:

(i) To calculate the electronic contribution to the defect formation free energies we employ the self-consistent first-principles full-potential linearized muffin-tin orbital (FP-LMTO) method¹⁸ and the local-density approximation. The LMTO method is well suited for compounds containing d electrons, such as $\text{Hg}_{1-x}\text{Cd}_x\text{Te}$.

(ii) Because the local-density approximation (LDA) overbinds, we have also employed gradient corrections to the LDA of the Langreth-Mehl-Hu type.¹⁹ These corrections greatly improve the overbinding found in the LDA.²⁰ We believe the calculated energies are precise enough that we may make comparison with atoms referenced to the free atom, and therefore by combining these energies with the translational energy of the atoms in the vapor phase, are able to calculate the chemical potential for a monoatomic mercury vapor.

(iii) A Green's function formalism within a valence force model plus point-charge ionic model is used to calculate the vibrational contribution to the defect formation free energy, both the enthalpy and entropy.

(iv) The combination of the electronic, translational, and vibrational free energies calculated in (i)–(iii) encompass the primary contributions to the total defect formation free energies when referenced to a mercury vapor. The total defect formation free energy is then incorporated into a quasichemical formalism,²¹ and predictions of absolute defect concentrations as a function of the thermodynamic variables temperature and pressure can be made.

The remainder of the paper is organized as follows. In Section II we describe the quasichemical formalism used to calculate the neutral native defect concentrations and its extension for ionized defects and alloys. The calculations of the defect formation free energies are discussed in Sections III and IV for the electronic and vibrational contributions, respectively. In Section V we present the results of our calculations and a comparison with available experimental results. We end with a brief summary and conclusions of our work in Section VI.

II. DEFECT CONCENTRATIONS

A. Quasichemical formalism in compounds

We begin by outlining the formalism employed to calculate the defect concentrations in a compound as a function of external parameters. In Section IIC we discuss extensions of the formalism necessary to treat the low- x alloy $\text{Hg}_{1-x}\text{Cd}_x\text{Te}$.

The defect reactions for the compound AC to be considered in this paper are listed in Table I. We have chosen the AC unit cell and A in the phase R as our reference states for the calculation of the reactions' free energies. From Gibbs' phase rule we know that for a system of two components (A and C) and two phases (one of which is the AC zincblende solid) there are two degrees of freedom. For this paper we shall assume that temperature is one degree and that the chemical potential of an external reservoir of A or C atoms is the other. The chemical potential is chosen to be consistent with the experimental situation to be modeled. We shall choose our reference state to be the mercury vapor and therefore choose to reference our reaction energies to the AC solid and A_R , which will be taken as the monoatomic mercury vapor (extensions of this analysis to the alloys are discussed in Section V).

Reference to other reservoirs can be obtained by considering the additional reaction



or for molecular species as the reference



where n_i is the appropriate integer, and by taking linear combinations of these with the reactions in Table I.

We are not restricted to specifying the temperature and a chemical potential of one of the species as the two degrees of freedom, but could choose instead another particular set, including, for example, the stoichiometry of the system.¹⁰ While other choices are possible, usually one does not know *a priori* the material's stoichiometry.

Assuming that the defect densities are small and that they are noninteracting, from the law of mass action we can write the reaction constant for each of the neutral defect reactions in Table I as^{21,22}

$$K_{X^\times} \equiv \theta \exp \left(-\frac{F_{X^\times}}{k_B T} \right) = [X^\times] \quad (2)$$

where $[X^\times]$ is the density of the neutral defect X , θ is the number of unit cells per volume and converts $[X^\times]$ from site fraction to defects per unit volume, and F_{X^\times} is the free energy for the neutral defect reaction. The free energy for any defect X can be written as the sum

$$F_X = F_X^{vib} + F_X^{elect} + F_X^{trans} + k_B T \ln(G), \quad (3)$$

where k_B is Boltzmann's constant and F_X^{vib} is the vibrational, F_X^{elect} is the electronic, and F_X^{trans} is the translational energy contribution to the reaction free energy, and G accounts for the degeneracies of the reactants. In the quasi-chemical approximation (QCA), $G = (g_C g_D)/(g_A g_B)$ for the reaction $A + B \rightarrow C + D$, where g_i is the degeneracy of reactant i . Once F_{X^\times} is known for a given reaction, K_{X^\times} can be evaluated and the defect concentration can be determined. The difficulty, of course, is in the evaluation of F_{X^\times} , which is discussed in Sections III and IV.

B. Ionized defects and the intrinsic reaction constant

The above discussion applies to the neutral defect densities. In most semiconductors the native point defect will have one or more localized levels in the band gap, allowing for multiple ionization states of the defect. We thus need to calculate the concentration of these ionized defects, in addition to the neutral concentrations discussed above, to obtain the total defect populations. Once the energies of the localized levels are determined (Section III E) their populations can be calculated via

$$\frac{[X']}{[X^\times]} = \frac{g_{X'}}{g_{X^\times}} \exp \left(\frac{\mu_F - E_a - F_{X'}^{vib} + F_{X^\times}^{vib}}{k_B T} \right) \quad (4)$$

for an acceptor and

$$\frac{[X^*]}{[X^\times]} = \frac{g_{X^*}}{g_{X^\times}} \exp \left(\frac{E_d - \mu_F - F_{X^*}^{vib} + F_{X^\times}^{vib}}{k_B T} \right) \quad (5)$$

for a donor state of the defect X . A bullet superscript indicates a positive charge and a prime a negative charge, E_a and E_d are the acceptor and donor one-electron ionization energies with respect to the valence and conduction band (both defined as positive for states in the gap), and μ_F is the Fermi energy. Although the last term in the exponential, $-F_{X'}^{vib} + F_{X^\times}^{vib}$, should rightly be there, and corresponds to the difference in the vibrational free energy of the neutral and ionized defect, it has never been considered previously and for the present we shall neglect it, too.

For multiply ionized defects with positive Hubbard U 's (reactions 7 and 8 in Table I), the above expression for the number of ionized acceptors generalizes to

$$\frac{[X^{z'}]}{[X^\times]} = \frac{g_{X^{z'}}}{g_{X^\times}} \exp (z\mu_F - E_a^1 - \dots - E_a^z - F_{X^{z'}}^{vib} + F_{X^\times}^{vib}) \quad (6)$$

where z is an integer and E_a^i is the ionization energy of the i^{th} ionization level. A similar generalization applies for the donor levels.

For each ionized defect concentration, we introduced one equation. In addition, though, we have two new unknowns, the Fermi energy and either the electron or hole concentration. Thus, two additional equations are needed.

First, we have the additional reaction for the generation of electron-hole pairs across the band gap, reaction 9 in Table I, and the corresponding intrinsic reaction constant

$$K_{pn} = [h^*][e'] = pn \quad (7)$$

where $p \equiv [h^*]$ and $n \equiv [e']$. In general, K_{pn} depends on the shapes of the conduction and valence bands, the band gap energy, the Fermi energy (for degenerate statistics), and the temperature variation of these quantities. Several limits are often encountered in the evaluation of K_{pn} . First, when the conduction and valence bands are parabolic, although not necessarily isotropic, $E \propto k^2$, and the reaction constant can be written in terms of the Fermi-Dirac integrals as

$$K_{pn} = 4 \left(\frac{2\pi k_B T}{h^2} \right)^3 (m_h m_e)^{3/2} \times \mathcal{F}_{1/2} \left(\frac{\mu_F - E_v}{k_B T} \right) \mathcal{F}_{1/2} \left(\frac{E_c - \mu_F}{k_B T} \right) \quad (8)$$

where $\mathcal{F}_{1/2}$ is the Fermi-Dirac function; E_c , E_v , and μ_F are the conduction band, valence band, and Fermi energies, respectively; m_h and m_e are the hole and electron density-of-states effective masses, respectively; and h is Planck's constant. In the nondegenerate limit, this reduces to the familiar expression

$$K_{pn} = 4 \left(\frac{2\pi k_B T}{h^2} \right)^3 (m_h m_e)^{3/2} \exp \left(\frac{E_v - E_c}{k_B T} \right) \quad (9)$$

which is independent of the Fermi energy. For the general case, which will apply even at moderate temperatures for narrow-gap HgCdTe, K_{pn} depends on the extrinsic carrier densities through its dependence on μ_F . Moreover, the conduction band in this narrow-gap material is not well represented by a parabola, but is rather more hyperbolic.²³ Because the hyperbolic dispersion relation approaches a linear dependence away from the band edge, we will for the present assume a linear dispersion relationship of the form $E = \alpha k$. In this case the intrinsic reaction constant becomes

$$K_{pn} = 2 \left(\frac{2\pi k_B T m_h}{h^2} \right)^{3/2} \frac{2}{\pi^2} \left(\frac{k_B T}{\alpha} \right)^3 \times \mathcal{F}_2 \left(\frac{\mu_F - E_v}{k_B T} \right) \mathcal{F}_{1/2} \left(\frac{E_c - \mu_F}{k_B T} \right) \quad (10)$$

where \mathcal{F}_2 is Fermi-Dirac integral of order 2.

The requirement of charge neutrality leads to a second additional equation:

$$\sum_i \sum_z z [X_i^{z'}] + [e'] = \sum_i \sum_z z [X_i^{z''}] + [h^*] \quad (11)$$

where i sums over the various defects and z sums over the various ionization states of the defect X_i .

C. Quasichemical formalism in alloys

We wish to generalize the above formalism to the ideal cation substituted pseudobinary alloy $A_{1-x}B_xC$. It is perhaps easiest to demonstrate the generalization with a specific defect reaction, for example a neutral vacancy on the cation sublattice. In the compound AC the formation reaction is given by reaction 1, Table I:



where V_α indicates a vacancy on the cation sublattice. In the alloy a neutral vacancy on the α sublattice can form via the same reaction. The only difference comes in the evaluation of the reaction constant. In the compound the vacancy density is given by

$$[V_\alpha^x] = \theta \exp \left(\frac{-F_{V_\alpha^x}}{k_B T} \right) \quad (13)$$

while in the alloy it is given by

$$[V_\alpha^x] = \theta(1-x) \exp \left(\frac{-F'_{V_\alpha^x}}{k_B T} \right) \quad (14)$$

where $-F'_{V_x}$ is the reaction free energy corresponding to Eq. (12) in the alloy. The factor of $(1 - z)$ results from the configurational entropy contribution to the chemical potential of A on a lattice site (ls), $k_B T \ln([A_{ls}]/[ls]) \simeq k_B T \ln(z)$. Because we have assumed that the defect concentrations are small, the configurational entropy contribution to the chemical potential of A in the compound AC is $k_B T \ln([A_{ls}]/[ls]) \simeq 0$. In both the compound and the alloy θ is the same.

In addition to Eq. (12), in the alloy the vacancy on the α sublattice can also form via the reaction



with

$$[V_{\alpha}^x] = \theta(x) \exp \left(\frac{-F''_{V_{\alpha}^x}}{k_B T} \right) \quad (16)$$

where $F''_{V_{\alpha}^x}$ is the reaction free energy corresponding to Eq. (15) in the alloy. Now the vacancy concentrations predicted by Eqs. (14) and (16) must be equal and thus

$$(1 - z) \exp \left(\frac{-F'_{V_x}}{k_B T} \right) = (z) \exp \left(\frac{-F''_{V_{\alpha}^x}}{k_B T} \right). \quad (17)$$

It is apparent that this simply corresponds to the difference of Eqs. (12) and (15)



that is, the exchange of an A and B on a lattice site, which is a reaction in the alloy in equilibrium with A_R and B_R . An analysis similar to the above applies for the anion antisite, C_{α} , which also substitutes on the cation sublattice.

In the pseudobinary alloy, the vacancy free energies F'_{V_x} and F'_{V_x} appearing in Eqs. (13) and (14) may be different. The energy of a vacancy depends on the local configuration of the surrounding lattice; this changes in the second and more distant neighbor shells for the cation vacancy and the anion antisite in the cation substituted alloys. A completely rigorous approach would treat each kind of vacancy uniquely; indeed in a previous work¹⁸ we found a configuration dependence of the vacancy in the $A_{0.5}B_{0.5}C$ lattice, of several tenths of an eV, varying approximately linearly in the number of A atoms in the second neighbor shell. Here, we have ignored this refinement and assumed the A vacancy and C antisite surroundings are totally of species A . This is justified to some extent because we are interested in low x compositions of $Hg_{1-x}Cd_xTe$.

For defects on the C sublattice (e.g., the anion vacancy and the cation antisites) as well as interstitial atoms in certain tetrahedral sites, one must more carefully consider the complications from the alloy, because disorder is found already for nearest neighbors. For systems in which these classes of defects are important, the configuration dependence of the surrounding sublattice must be taken into account. For low x $Hg_{1-x}Cd_xTe$ we find the densities of these defects to be quite low, and thus the error incurred in using the electronic energies calculated for the pure AC compound will not impact the major conclusions of our work.

Finally, the band gap is one other important consideration when comparing the alloy to the pure compound. This is of particular importance for the intrinsic reaction constant and we employed an empirical fit to the temperature dependence of the alloy band gap and intrinsic carrier concentration that are used to calculate K_{pn} . This is presented in detail in Section III G.

III. CALCULATION OF DEFECT FORMATION FREE ENERGY: ELECTRONIC CONTRIBUTION

A. Full potential LMTO calculations

Total energy calculations for the defect reactions were all obtained with a full-potential version²⁴ of the LMTO method, in the local density functional approximation of Barth and Hedin.²⁵ This method has been tested extensively for most of the elemental sp and d bonded solids, the II-VI, III-V and column IV semiconductors, and a host of other solids. Our results, which will be reported elsewhere,²⁰ show good agreement with experiments for all systems studied, with small and systematic errors in structural and mechanical properties. The most prominent error, particularly for the present purposes, is the overbinding of the solid.

In the FP-LMTO method, the only important approximation we make beyond the local-density approximation, lies in the treatment of the interstitial matrix elements. The LMTO method employs an atom-centered basis, represented by Hankel functions in the interstitial. For the calculations presented here, the basis consisted of a "triple kappa" basis 22 orbitals per atom, with energies -0.01 , -1 , and -2.3 Ry for the s and p orbitals, and -0.01 and -1 Ry for the d . Inside the muffin-tin (MT) spheres, wave functions are represented by spherical harmonics and numerically tabulated radial functions. The electron density and potential can be similarly represented, since the density generated by a Hamiltonian is obtained by summing over the eigenvectors. Outside the MT spheres, another treatment is necessary. Methfessel²⁶ developed a simple, efficient way to represent the density and potential in the interstitial by extrapolation from the edges of MT spheres, where the value is well known. The electron density is represented in the interstitial as a linear combination of Hankel functions that are chosen to match the value and slope of the function at each MT sphere. Two Hankels per site and lm are enough to match the values and slopes at all MT spheres. This representation of the density throughout the interstitial is approximate, although it becomes exact near any MT sphere. Extensive tests show that the approximation works very well for close-packed systems, but the errors can become significant when the packing is poor. To ensure a good fit to the charge density and potential in the interstitial region of the zincblende solids, we include empty spheres at each tetrahedral interstitial site (rendering the sphere packing bcc for the ideal lattice). In addition, we added orbitals to the basis by centering them on the empty spheres. Addition of $2s$ and $2p$ orbitals changed the energy by approximately 0.1 mRy/atom, showing that the basis is nearly complete.

To assess the validity of the interstitial approximation for the representation of the charge density and interstitial matrix elements, an alternative approach was developed,²⁴ which is similar to a procedure described by Jones.²⁷ When calculated in this way the total energies changed by approximately 1 mRy/atom, showing that the approximation is a good one.

Both the charge density inside the spheres and the tails of Hankel functions centered on a neighboring sphere were expanded to $l = 6$. We estimate that the error introduced by truncation at $l = 6$ to be about 1 mRy/atom, in line with other errors in the method. The core was allowed to relax during the self-consistency cycle. The semicore d electrons in the tellurium were treated explicitly as valence states in a second panel; explicit treatment of these states was found to introduce a small but significant correction to the total energy. For the 16-atom cells, the Brillouin zone integrals were done by a sampling method for the charge density, and the linear tetrahedron method for the band-structure energy, augmented by Blöchl weights, and a mesh of four divisions was used (6 k-points). Checks showed that this was sufficient to converge the energy to 1 mRy/cell.

B. Supercell approximation

Supercells are used in which a periodic array of defects is constructed. Defect formation energies are calculated from a difference in total energies of the compound with and without the defect. For example, if we denote $\mathcal{E}_j(V_A)$ as the energy of a supercell containing j lattice sites and one A vacancy, the energy for defect reaction 1 in Table I is given by

$$E(V_A) = \mathcal{E}_j(V_A) + E(A_R) - \mathcal{E}_j(AB) \quad (19)$$

where $E(A_R)$ is the energy of an A atom in the reference state R and $\mathcal{E}_j(AB) = jE(AB)$ where E_{AB} is the energy of an ideal AB unit cell. For some defects the number of lattice sites changes in the reaction; for example for the formation of the B antisite via reaction 4 in Table I, the formation energy is given by

$$E(B_A) = \mathcal{E}_j(B_A) + 2E(A_R) - \mathcal{E}_{j+2}(AB). \quad (20)$$

Because we wish to calculate the formation energies in the dilute limit, we use the largest supercell computationally feasible. For this paper, all calculations were done using 16-atom supercells.

C. Gradient corrections to the local density

The local-density approximation generally overbinds the solids. Several systematic extensions of the local-density function have been proposed that are based on generalized gradient approximation for the exchange and correlation energies. We have considered one of these extensions, that proposed by Langreth and Mehl,¹⁹ and have examined the systematics in the gradient corrections to the lattice constants, cohesive energies, bulk modulus, and other elastic constants for a wide array of solids²⁰; preliminary results of that work for the zincblende semiconductors are shown in Table II. With few exceptions, the gradient correction systematically improves the prediction of the cohesive energy,

although the prediction of the elastic constants often worsens slightly. The improvement in the cohesive energy is largely due to improvement in the calculation of the total energy of the free atoms, rather than the solid.

Here, we are interested in calculating total energies for reactions in which a constituent is exchanged between the solid and the vapor, and thus the errors inherent in the local-density calculation of the cohesive energy will be present in these energies also. Because the relaxations do not change significantly when gradient corrections are added, we have completed the majority of the calculation, including the relaxation, within the FP-LMTO. The gradient correction energy, calculated at the LDA-determined relaxed positions, is then added to the LDA energy.

D. Relaxation

In general the lattice relaxes in the presence of a defect, thereby lowering the lattice energy. In the dilute defect limit, the radial relaxation of the lattice extends to infinity.²⁸ In the supercells we account for this relaxation by allowing the overall lattice constant of the supercell to relax to minimize the supercell total energy. Because HgTe and CdTe are nearly lattice matched, and their elastic constants are the same, the defect relaxations in pure HgTe should be comparable to those in the HgCdTe alloys. Second, for the most important defects, we permit the radial relaxation of the defect near-neighbor atoms. For the on-site defects (the vacancies and antisites) we permit only the nearest-neighbor atoms to relax. Estimates of these relaxation energies are given in Section V.

Relaxation energies are calculated only for the neutral defects and are assumed comparable in the ionized defects. Nonradial relaxations such as the trigonal and tetragonal distortions that split the degeneracy of the triply degenerate T_2 states may be important and may differ substantially for the different charge states of the system. Because the symmetry of the distortion depends on the charge state of the defect, distortions and charge states must be treated simultaneously. These distortions have not been considered in this paper.

E. Localized defect levels

The calculation of the ionization states of the defects is perhaps the most difficult part of the calculation of the native defect concentrations, in large part because of the inadequacies of the LDA in predicting the band gap of the semiconductors. This is additionally complicated by the fact that our calculations were done for HgTe, which is known experimentally to be a semimetal with a negative band gap of -0.3 eV, so that even if the LDA band gap were correct, we would still have a zero-gap material. Furthermore, because the Coulomb fields associated with a defect may be extended, we expect that very large supercells will be needed to isolate the localized levels of an individual defect.

We have developed a method to calculate the location of localized defect levels in the band gap and have applied it to the arsenic antisite defect in GaAs. This defect was chosen because of its technological importance and because these levels have been determined experimentally by Weber et al.²⁹ Calculations were done within the ASA so that we could examine the convergence of our results going to large (128 atom) supercells. Our approach is similar to that discussed by van der Waal et al.³⁰ in which the shift in the Fermi level is examined as electrons are added to (or removed from) the defect, with a compensating uniform background charge added so as to maintain charge neutrality. We find good agreement with experiments of the two antisite donor levels. We also have found these energies agreed closely with the positions of peaks in the density of states, when referenced to the top of the valence band. Details of the calculation will be given elsewhere.

Because the compositions of HgCdTe of interest here have narrow band gaps, the determination of the exact location of the defect levels in the band gap is not as important for the purpose of calculating the defect concentrations as in a wider-gap semiconductor such as GaAs, although the identification of the position of defect levels is useful in understanding mechanisms limiting carrier lifetimes. We have used the 54-atom supercells of HgTe to determine the type (acceptor or donor) of the various native defects based on the position of the Fermi level with respect to the states that lie within ~ 0.1 eV above the valence band edge. In addition, an assessment of whether the state is a single or double donor or acceptor and whether the state is shallow or deep has been made based on the position of the density of states peaks. For the mercury vacancy, we follow the arguments of Cooper and Harrison,³¹ and assume that it is a negative-U center, with the neutral and double acceptor states being the only observable states; this assumption is consistent with the observation that the mercury vacancies are always found to be doubly ionized acceptors.¹

F. Ionization state degeneracy

The degeneracy of the various ionization states of each defect may differ and must be determined³² to complete the calculation of the density of ionized defects. As an example, we consider the *A* vacancy in a II-VI material, and use tight-binding language for the purpose of discussing the defect states. There are four dangling anion hybrids, each donating 1.5 electrons to the system, for a total of six electrons at the vacancy site. Although we have not explicitly calculated it, for the purpose of computing state degeneracy, we assume that a symmetry lowering Jahn-Teller distortion will take place whenever there is a state degeneracy beyond two (for spin) and a partial occupancy of that state. Thus, we assume that the highest filled vacancy level in the neutral state is doubly occupied with one electron spin-up and one spin-down, and that the level can accept no other electron. Because there is only one unique configuration for this state, the state has a degeneracy of one. For the single acceptor state in which one electron has been added to the vacancy, the extra electron can either go in spin-up or spin-down, with equivalent energies. The degeneracy of the state is therefore two. Finally, if the vacancy is a doubly ionized acceptor, the lowest energy configuration for the two additional electrons is with one spin-up and one spin-down, with a net state degeneracy of one. This assignment of degeneracies – one, two, and one for the neutral, singly ionized, and doubly ionized acceptor, respectively – will hold even if the state is a Hubbard negative-*U* state, although in this case, the singly ionized state will not be occupied.

A similar argument follows for the other donor and acceptor defect levels. In general, for the II-VI materials we find a degeneracy of one for the neutral defect state, two for the singly ionized state, and one for the doubly ionized state.

G. Intrinsic reaction constant

We are interested in calculating native point defect densities at the relatively high temperatures at which equilibration occurs. It is difficult to calculate K_{pn} theoretically because of the difficulty in calculating the finite-temperature band structure; in general the band gap and the conduction and valence band shapes are all temperature dependent. An additional complexity in calculating K_{pn} in low *x* $\text{Hg}_{1-x}\text{Cd}_x\text{Te}$ is the nonparabolicity of the conduction and light-hole bands near their extrema.²³

For the purposes of evaluating the defect concentrations, we have calculated K_{pn} using Eq. (10) with $m_h^* = 0.443^{33}$; an empirical relationship for the dependency of the band gap on composition, *x*, and temperature³⁴

$$\begin{aligned} E_g(x, T) &= E_c - E_v \\ &= -0.302 + 1.93x - 0.810x^2 + 0.832x^3 \\ &\quad + 5.35 \times 10^{-4}T(1 - 2x), \end{aligned} \quad (21)$$

which was fit for $4.2 \leq T \leq 300$ K; and a linear dispersion relationship for the conduction band with α chosen to yield good agreement with experimental values of the intrinsic carrier concentrations³³ for $T < 400$ K. We assume that the intrinsic reaction constant thus computed is valid at temperatures up to 655°C, although there have been no measurements above ~400 K to substantiate this extrapolation.³⁵

IV. CALCULATION OF DEFECT FORMATION FREE ENERGY: VIBRATIONAL CONTRIBUTION

When a defect is introduced into the lattice, the vibrational modes of the system are modified. We must include in our calculation of the defect formation free energy a term that comes from modifications of the vibrational spectrum. Most authors neglect this contribution to the formation free energy. As we will see in Section V, although the electronic contribution to the free energy is dominant, the vibrational changes can be significant and they make a substantial impact on the calculated magnitude of the defect concentrations.

Although ideally the vibrational contribution to the formation energy should be calculated within LDA on the same footing as the static electronic contribution, including all of the anharmonic terms, this is a difficult and computationally demanding task. Instead, we take an alternative approach and calculate the vibrational spectrum of the zincblende lattice using Keating's valence force-field model for the short-range elastic interactions.³⁶ Although experimental elastic constants were used, LDA theory actually predicts the elastic constants within 10% for HgTe and CdTe, so we could equally well have used the calculated values. Because we are dealing with an ionic crystal, we have included a point-charge model to account for the Coulombic interactions.³⁷ Unlike the valence force-field contributions to the dynamical matrix, the Coulomb contributions are long-range in nature and induce a macroscopic

electromagnetic field, which results in a screening of the transverse optical phonons. The ionic charge is chosen to yield agreement with experiments for the zone center splitting of the transverse and longitudinal optical phonons. A Green's function approach is used to evaluate the lattice-defect induced modifications to the phonon spectrum; from the perturbed phonon density of states the change in the vibrational free energy can be calculated. Like the electronic energies, the calculations were done for pure HgTe and are assumed applicable to defect calculations in $\text{Hg}_{0.8}\text{Cd}_{0.2}\text{Te}$. We expect that this is a reasonable assumption because the elastic constants for HgTe and CdTe are nearly identical. In this paper we only consider the vibrational free energy of the neutral defects and assume

$$F_{X^{\cdot\cdot}}^{\text{vib}} \approx F_{X^{\cdot}}^{\text{vib}} \approx F_{X^0}^{\text{vib}} \quad (22)$$

for all ionization states. Details of the calculations are given in the Appendix. Preliminary results of this model were given previously.^{14,17}

V. RESULTS AND DISCUSSION

A. Formation free energies in HgTe

Calculated defect formation electronic energies in HgTe for the defect reactions listed in Table I and with A_R as the free mercury atom, are listed in Table III. For all defects, the gradient correction for the 16-atom supercell is calculated for the relaxed configuration, as determined by the LDA calculation.

Although the total electronic formation energies listed in Table III are important contributions to the formation free energy, these energies alone cannot be used to assess the relative importance of the various defects in the solid. This is mostly due to the free energy of the atom in the reference state (in excess of its free atom electronic energy) that is not included in these electronic energies, and which is discussed in the next section. This point should be obvious because we could have just as well defined our defect reactions with respect to the tellurium molecule in the vapor phase and the HgTe solid, and obtained the corresponding reaction energies that would be quite different from those in Table III.

The calculated phonon dispersion curve for HgTe is given in Fig. 1, and is in fair agreement with the experimental results. The discrepancies with the experimental curves, in particular near the Brillouin zone boundary, can be attributed for the most part to our neglect of long-range elastic interactions in the near-neighbor valence force-field model.³⁸ The vibrational entropy and energy contribution to the defect formation free energy are calculated from the density of phonon states; results at 500°C are given in Table IV. Eq. (A20) can be used to estimate the values at other (high) temperatures.

B. Defect reaction constants in $\text{Hg}_{0.8}\text{Cd}_{0.2}\text{Te}$

The reaction constants for each of the defect reactions listed in Table I are calculated as a function of temperature, where the reference state was taken as the monoatomic mercury vapor at pressure P_{Hg} . Electronic energies for the neutral defect formation energies are taken from Table III. Vibrational free energies are calculated using the general temperature expression, as discussed in the Appendix, although for the purpose of obtaining an analytical expression for the reaction constants with the primary temperature dependency explicitly displayed, we have fit our results for 500°C to the high-temperature expression, Eq. (A20).

A third contribution to the formation free energy comes from the free energy of the mercury in the reference state, less the electronic energy of the free mercury atom that is contained in the electronic defect formation energies. For the vapor, we must include the translation free energy of the atoms. The chemical potential for monoatomic mercury in the gas phase is given by the standard expression from statistical mechanics

$$\mu_{\text{Hg}} = kT \ln \left(\frac{P_{\text{Hg}}}{kT} \left(\frac{h^2}{2\pi m_{\text{Hg}} kT} \right)^{3/2} \right) \quad (23)$$

Combining these three contributions to the reaction free energy we obtain the reaction constants for each of the defect reactions. For example, for the neutral mercury vacancy in HgTe, we obtain

$$K_{V_{\text{Hg}}} = [V_{\text{Hg}}^{\cdot}] = \theta(1-x) \frac{kT}{P_{\text{Hg}}} \left(\frac{2\pi m_{\text{Hg}} kT}{h^2} \right)^{3/2} (1.27 \times 10^6 T^{-3}) \exp \left(\frac{-2.09 \text{ eV}}{kT} \right). \quad (24)$$

where we have taken $g_{V_{\text{Hg}}} = 1$, $-F_{V_{\text{Hg}}}^{\text{elect}} = -2.09$, $\theta = 1.48 \times 10^{22} \text{ cm}^{-3}$, and where we have replaced $\exp(-F^{\text{el}}/k_B T)$ by $\exp(-(-0.2 \text{ eV} + 8.9 k_B T)/k_B T)|_{800^\circ\text{C}} \approx 1.27 \times 10^6 T^{-3}$. Reaction constants for the eight native point defects considered in this paper are listed in Table V.

The reaction constants for the ionized defects are calculated using Eq. 6 for acceptors and its generalization for donors. We define

$$\begin{aligned} K_{X^{+}} &= [X^{+}] = [X^{\times}] \frac{g_{X^{+}}}{g_{X^{\times}}} \exp(z\mu_F - E_a^1 - \dots E_a^s) \\ &= K_{X^{\times}} \frac{g_{X^{+}}}{g_{X^{\times}}} \exp(z\mu_F - E_a^1 - \dots E_a^s) \end{aligned} \quad (25)$$

and

$$K_{X^{s+}} = [X^{s+}] = K_{X^{\times}} \frac{g_{X^{s+}}}{g_{X^{\times}}} \exp(E_d^1 + \dots + E_d^s - z\mu_F). \quad (26)$$

C. Defect concentrations in $\text{Hg}_{0.8}\text{Cd}_{0.2}\text{Te}$

Gibbs' phase rule tells us that for a system of three components (A, B, and C) and two phases (zincblende solid and vapor) there are three degrees of freedom. In evaluating the defect concentrations in $\text{Hg}_{0.8}\text{Cd}_{0.2}\text{Te}$ we have chosen the temperature, the mercury pressure P_{Hg} , and the alloy composition x as these specified variables; the tellurium and cadmium pressures, the crystal stoichiometry, and the density of the various native point defects are determined by these conditions.

The reaction constants in Table V are evaluated to determine the concentrations of the various native point defects as a function of temperature and pressure. The Fermi energy is determined by requiring charge neutrality. The activation energies for the shallow donor and acceptor states are taken to be zero; the sensitivity of our results to this assumption is discussed further below.

Figs. 2(a)–(c) show the defect concentrations at various equilibration temperatures. Pressure ranges are chosen so as to stay within the stability region of the material.⁶ At all temperatures and pressures considered, the dominant defect is found to be the doubly ionized mercury vacancy, in agreement with previous interpretations of experiments¹; our result confirms the generally accepted experimental observation that the mercury vacancy is responsible for the p-type behavior of undoped HgCdTe equilibrated at high temperatures.

At all temperatures, the second most dominant defect is found to be the tellurium antisite. The antisite concentration decreases more rapidly with P_{Hg} than does the mercury vacancy, and thus is most important at low mercury pressures. As does the mercury vacancy, the tellurium antisite defect accommodates excess tellurium in the lattice, and therefore its presence also shifts the stoichiometry towards the tellurium-rich side of the phase diagram.

The reason the tellurium antisite concentrations is so high deserves comment. The tellurium antisite formation energy is larger than that for the mercury vacancy by 1 eV (Table III). However, as can be seen from Table V, the pre-exponential factor of the reaction constant for the tellurium antisite is enormous. The large pre-exponential factor results from the large phase space factor (entropy) gained by creating two free mercury atoms compared to that lost by elimination of a formula unit. In contrast, the mercury antisite density is low, despite the fact that its formation energy is quite small; this again is a result of the pre-exponential factor that in this case is very small. Thus, it is clear that one must be cautious in deducing the relative populations of the various defects based on the electronic contributions to the defect formation energies alone.

While the tellurium antisite is never found to be the dominant defect controlling the doping under equilibrium conditions, it can introduce significant compensation at low mercury pressures. Moreover, the diffusion coefficient of the antisite is expected to be quite small because the diffusion of an antisite will necessarily involve at least one additional point defect, such as the mercury vacancy or the tellurium interstitial. Thus, the tellurium antisite may not reach equilibrium densities for the times and temperatures corresponding to the $\text{Ic } \tau$ -temperature ($\sim 250^\circ\text{C}$), high-mercury-pressure anneals typically employed to reduce the mercury vacancy density. If tellurium antisite densities are in fact equilibrated at a temperature at which the antisite diffusion effectively stops during cool-down from the growth temperature, then the antisites may be frozen-in at higher, nonequilibrium concentrations. If such a freezing-in of nonequilibrium antisites does occur, the tellurium antisite may in fact be the "universal" residual donor observed in densities of $\sim 10^{14} \text{ cm}^{-3}$ in material subjected to a low-mercury-pressure, high-temperature anneal, although it is not clear why, for example, the frozen-in density of antisites would be the same for LPE material grown from both mercury- and tellurium-rich melts. The tellurium antisite may also be the defect responsible for the n-type carrier concentrations in as-grown MBE material,⁸ which is believed to be grown on the tellurium-rich side of the phase diagram where antisite populations are highest.

Annealing strategies for reduction of the tellurium antisite densities can be developed, and may be important if the antisite is the residual donor. Consider, for example, a two-temperature annealing process in which a first anneal is done under mercury-saturated conditions, but at the lowest temperature for which the antisite is able to equilibrate in reasonable times. This anneal would serve to lower the antisite densities as much as possible. A second anneal would be much like that currently employed, - that is, at $\sim 250^\circ\text{C}$ under mercury-saturated conditions, - and would serve to anneal out the mercury vacancies, leaving the antisite densities effectively unchanged.

At 500°C mercury interstitials are present at levels $\approx 10^{10} \text{ cm}^{-3}$ and at no temperatures are present at levels high enough to significantly compensate the mercury vacancies, much less to turn the material n-type under equilibrium conditions. Unlike the tellurium antisites, the mercury interstitials are relatively fast diffusers,² and thus it is unlikely that nonequilibrium densities of interstitials will be frozen-in. The mercury interstitial densities that we predict are in quantitative agreement with those needed to explain the diffusion in $\text{Hg}_{1-x}\text{Cd}_x\text{Te}$ in the process simulator developed by Meléndez and Helms.³⁹ There is some uncertainty in the quantitative predictions of the mercury interstitial densities reported here because of the neglect of the alloy effects that we expect to be more significant than for the mercury vacancy and tellurium antisite. Although this correction will be largest for the mercury interstitial surrounded by four mercury first neighbors, it should also be significant for the interstitial surrounded by four tellurium first neighbors because of the six cation second-nearest neighbors, which are only slightly more distant than the first neighbors.

The mercury antisite and the tellurium vacancy and interstitial densities are all quite low, never exceeding $\sim 10^8 \text{ cm}^{-3}$ at 500°C . The corrections to these predicted densities may be sizable because of alloy effects, but such corrections should not significantly impact the densities of the mercury vacancy and tellurium antisite.

Fig. 2 shows the defect concentrations at the temperatures at which equilibration takes place; in Fig. 3 we show the defect concentrations for material equilibrated at 500°C , then quench cooled to 77°C . We have assumed that the total defect concentrations are frozen-in during the quench - for example $[V_{\text{Hg}}]_{\text{total}} = [V_{\text{Hg}}^x] + [V_{\text{Hg}}'] + [V_{\text{Hg}}'']$ is constant - but that the electrons and holes are allowed to reach a new equilibrium corresponding to the low temperature. Fig. 4 shows the low-temperature hole concentrations for such quench-cooled materials as a function of P_{Hg} and T_{anneal} , compared with the experimental results of Vydyanath.¹ The agreement of our theoretical results with the experiments is remarkably good considering that our calculated results are obtained almost entirely from first principles. Moreover, there is a significant uncertainty in the quenching efficiency of the experiments; thus, exact agreement with the experiments is not a valid criterion for testing the accuracy of the theory.

From Fig. 4 one can see that for the higher annealing temperatures our calculations predict a different dependence of hole concentration on the mercury pressure than is experimentally observed. The lower slopes for the theory result from our finding that the material is extrinsic at the higher temperatures. If the material is intrinsic when equilibrated as the experiments indicate, then $[V_{\text{Hg}}'']_{\text{hi}} \propto P_{\text{Hg}}^{-1}$, as can be obtained from Table V, with μ_F independent of $[V_{\text{Hg}}]$. However, if the material is extrinsic when equilibrated - that is, with $[h^*] = 2[V_{\text{Hg}}'']$ - then from the reaction



we see that $[V_{\text{Hg}}''] [h^*]^2 \propto [V_{\text{Hg}}'']^3 \propto P_{\text{Hg}}^{-1}$.

The discrepancies between theory and experiments may be due to a number of factors. First, both uncertainty in the quenching efficiencies and analysis of the Hall data may account for some of the discrepancy. There are also a number of uncertainties in the theoretical calculation that may account for the discrepancies. These include uncertainties in the electronic and vibrational defect formation free energy, the ionization energies of the defects (which were assumed to be zero in the above calculations), alloy effects, and finally the uncertainties in the intrinsic reaction constant. These are discussed in turn below.

First it is interesting to examine the sensitivity of our predictions to the accuracy of electronic and vibrational defect formation free energy. In Fig. 5 we have recalculated the 77 K hole concentrations as a function of the annealing temperature with the electronic contribution to the mercury vacancy formation energy increased by 10%, and a rigid shift upwards in our results by a factor of 2.5; such small changes result in better agreement with experiments. The corrections to our calculated mercury vacancy and tellurium antisite formation energies due to alloy effects have not yet been included in these calculations and are expected to be in the range of tenths of an eV, as discussed in Section IIC, and thus may account for the magnitude of correction used in this example. Preliminary estimates for the corrections for going from the 16-atom to the 32-atom supercell are $\sim 0.1 \text{ eV}$ for the cation vacancy and the tellurium antisite as well. Finally, Jahn-Teller relaxation energies have not been included in the present work and they may modify the electronic formation free energies. An increase in the effective vibrational frequencies ($\bar{\omega}$ in Eq. (A20)) can account for an upward shift in the densities. Such an increase may arise from differences between the neutral and ionized defect vibrational free energies and, perhaps, anharmonic effects that may be large at defects such as the vacancy where an atom is missing from the lattice. Thus, we see that our calculations agree with the experimental data approximately to within the known uncertainties of the theory.

Our results are also very sensitive to the intrinsic reaction constant, which in turn depends sensitively on the band structure and its temperature dependence. HgCdTe is known to be anomalous in that its band gap is found to increase with temperature at room temperature and below, and although there is no experimental information on the temperature dependence of the gap at higher temperatures, we have assumed that Eq. (21) extrapolates to higher temperatures. In addition, as discussed above, we have assumed a parabolic valence band, but a linear variation of the conduction band, with the slope chosen to agree with the intrinsic carrier concentrations [with the energy gap given by Eq. (21) at temperatures below 400 °C]. While this fit is quite good for the temperature range over which it is fit (from 77 K to 400 K), the reliability of K_{pn} at 250°C and above for which we have presented our defect density predictions is unknown. To demonstrate the sensitivity of our results to the intrinsic reaction constant we have calculated the 77 K temperature hole concentrations with the conduction band density of states increased a factor of ten and have found, except at the very highest temperatures, that the calculated hole concentrations vary as P_{Hg}^{-1} indicating intrinsic behavior at the annealing temperature, and resulting in better agreement with experiments. Because our results depend sensitively on the intrinsic reaction constant, it is essential to establish a reliable prediction of its value at the annealing and growth temperatures where equilibration of the defect densities takes place.³⁵

We have suggested that nonequilibrium densities of tellurium antisites may be the residual donor, but they may also be important SRH recombination centers. It is experimentally observed that the residual donor does not freeze out even for samples cooled to 4 K, and therefore its first ionization state must resonate in the conduction band. A SRH recombination center in $Hg_{1-x}Cd_xTe$ with $x = 0.22$ lies ~25 meV below the conduction band edge, has a larger capture cross section for electrons than holes, and typically has a density smaller than, but comparable to, the residual donor density. The properties of the antisite are consistent with such a level: it is a donor; although we have assumed here it is a single donor, it is likely that a second donor level is present in the gap and may be ionized at the high processing temperatures; and the first ionization level may be resonant in the conduction band, although we are unable to resolve this in our present calculations with certainty. A more quantitative prediction of the ionization levels of the antisite is needed to correlate it with a SRH center.

A technologically important step in making IR detectors from $Hg_{1-x}Cd_xTe$ is a low-temperature mercury-saturated anneal that is done to reduce the mercury vacancy concentrations. In Fig. 6 we show the defect concentrations for material annealed at various temperatures along the mercury-saturated side of the phase diagram. In such mercury-saturated anneals, if equilibrium can truly be reached, then the mercury vacancies will certainly be the dominant defect, with the tellurium antisite density being negligible. However, as discussed above, it is unlikely that equilibrium densities of antisites will be achieved at these relatively low temperatures.

The above analysis of defect concentrations can be repeated for a number of different situations. For example, we can calculate the native defect densities with a donor or acceptor impurity present. At the high growth temperatures, the impurity concentrations would have to be comparable to the vacancy concentrations to modify the high temperature vacancy concentration. On the other hand, even impurity densities of the order of $\sim 10^{15} \text{ cm}^{-3}$ will alter the native defect concentrations subjected to a low-temperature post-growth anneal. We can also repeat the above calculations for reference state other than the mercury vapor. For example, in HgCdTe tellurium precipitates are known to form as a metastable state upon cooling from high growth temperatures.⁴⁰ In the vicinity of a precipitate, the native defect populations will be in local equilibrium with the tellurium solid, and defect concentrations for this reference state can be calculated. Because this constitutes a nonequilibrium situation, one must address diffusion rates to assess the extent of the modified defect atmosphere about a precipitate.

VI. SUMMARY AND CONCLUSIONS

We have made quantitative predictions of the native point defect densities in $Hg_{0.8}Cd_{0.2}Te$ as a function of temperature and pressure and find good agreement with the available experiments. We have substantiated the claim that the primary defect is the mercury vacancy, and have identified the tellurium antisite as an important secondary defect. A first-principles approach was used for most of the quantities calculated, with the only significant empirical data being those needed to obtain the temperature-dependent intrinsic reaction constant.

Although we predict the undoped material to be always p-type, refinements in our calculations may show that the antisite may dominate in the low-mercury-pressure region and turn the material n-type by a native defect; our current accuracy is not sufficient to establish this. While most anneals of technological importance are done under mercury-saturated conditions to reduce mercury vacancy concentrations, exploration of the tellurium-saturated region where we predict the tellurium antisite densities become comparable to those of the mercury vacancy may help confirm the presence of tellurium antisites.

A second means to explore the presence of tellurium antisites and their relationship to the residual donor is through a careful set of experiments using two temperature anneals, as discussed above. Because we do not know the temperature

at which diffusion of tellurium effectively stops, the temperature of the first anneal would have to be varied, as would the annealing time; the mercury pressure could also be varied, although mercury-saturated conditions are those one would eventually want to employ. The identification of the tellurium antisite as the residual donor can be made if the donor densities in identically grown material were found to differ after the second anneal (using the standard conditions for a mercury-saturated low-temperature anneal) depending on the conditions of the first anneal. A quantitative analysis of this experiment would be quite difficult because, in addition to uncertainties in the temperature at which the tellurium antisite equilibration stops, if the tellurium antisite diffuses via a vacancy mechanism, the diffusion of the antisite will depend on the concentration of mercury vacancies present during the first anneal.

It would also be useful to perform high-temperature annealing as was done by Vydyanath,¹ but instead of quenching to 77 K and having to address the issue of quenching efficiency, follow the anneals by Hall analysis at the anneal temperature. Recently, an attempt at such an experiment was made by Wienecke *et al.*,³⁵ although analysis of such an experiment requires knowledge of the high-temperature intrinsic reaction constant.

ACKNOWLEDGMENTS

We wish to acknowledge the work of Michael Methfessel in development of the first-principles codes applied in this work. This work has been supported by NASA Contract NAS1-18226, ARPA Contract MDA972-92-C-0053, and ONR contract N00014-89-K-132. Computational support was provided by the Numerical Aerodynamical Simulation computing facility at NASA Ames Research Center.

APPENDIX: VIBRATIONAL ENTROPY OF POINT DEFECTS IN SEMICONDUCTORS

As discussed by Keating,³⁶ we assume the elastic energy for a zincblende structure can be written as

$$V = \frac{3\alpha}{8d_0^2} \sum_i (\Delta(\vec{r}_i \vec{r}_i))^2 + \frac{3\beta}{8d_0^2} \sum_{i>i'} (\Delta(\vec{r}_i \vec{r}_{i'}))^2 \quad (A1)$$

where i and i' sum over all bonds, $\Delta(\vec{r}_i \vec{r}_{i'}) = \vec{r}_i \vec{r}_{i'} - \vec{r}_i^0 \vec{r}_{i'}^0$, with \vec{r} and \vec{r}^0 the bond vectors connecting adjacent atoms in the distorted and equilibrium lattices, respectively. For first-neighbor interactions, the sum in the second term runs over only those bonds connected to a common atom.

For a nonionic material, the normal modes for the displacement of the atoms are determined by solving the equation of motion for the lattice cast in the usual manner in terms of the three-dimensional eigenvalue equation

$$\omega^2 \vec{u} = \mathbf{D}^*(\mathbf{k}) \vec{u}. \quad (A2)$$

Here, $\mathbf{D}^*(\mathbf{k})$ is the (elastic) dynamical matrix and

$$\vec{u} = \begin{pmatrix} \vec{u}_1 \\ \vec{u}_2 \end{pmatrix} \quad (A3)$$

is the polarization vector of the normal modes, where \vec{u}_i is the displacement vector of the i^{th} atom. For the zincblende lattice there are two atoms per unit cell, so $i=1$ or 2 .

In terms of the elastic constants, C_{11} and C_{12} , the dynamical matrix for the valence force field model is given by

$$\mathbf{D}^*(\vec{k}) = \begin{pmatrix} \frac{8dC_{11}}{\sqrt{3}m_1} \mathbf{I} & \frac{2dC_{12}}{\sqrt{3}m_1 m_2} \mathbf{S}(\vec{k}) + \frac{2d(C_{11}-C_{12})s(\vec{k})}{\sqrt{3}m_1 m_2} \mathbf{I} \\ \frac{2dC_{12}}{\sqrt{3}m_1 m_2} \mathbf{S}^*(\vec{k}) + \frac{2d(C_{11}-C_{12})s^*(\vec{k})}{\sqrt{3}m_1 m_2} \mathbf{I} & \frac{8dC_{11}}{\sqrt{3}m_2} \mathbf{I} \end{pmatrix} \quad (A4)$$

where d is the equilibrium bond length, m_1 and m_2 are the masses of the two atoms in the unit cell, \mathbf{I} is the 3×3 unit matrix, and \mathbf{S} is given by

$$\mathbf{S} = \begin{pmatrix} s_1 & s_4 & s_3 \\ s_4 & s_1 & s_2 \\ s_3 & s_2 & s_1 \end{pmatrix} \quad (A5)$$

with

$$s_1(\vec{k}) = e^{i\vec{k}\vec{d}_1} + e^{i\vec{k}\vec{d}_2} + e^{i\vec{k}\vec{d}_3} + e^{i\vec{k}\vec{d}_4}, \quad (\text{A6a})$$

$$s_2(\vec{k}) = e^{i\vec{k}\vec{d}_1} + e^{i\vec{k}\vec{d}_2} - e^{i\vec{k}\vec{d}_3} - e^{i\vec{k}\vec{d}_4}, \quad (\text{A6b})$$

$$s_3(\vec{k}) = e^{i\vec{k}\vec{d}_1} - e^{i\vec{k}\vec{d}_2} + e^{i\vec{k}\vec{d}_3} - e^{i\vec{k}\vec{d}_4}, \quad (\text{A6c})$$

and

$$s_4(\vec{k}) = e^{i\vec{k}\vec{d}_1} - e^{i\vec{k}\vec{d}_2} - e^{i\vec{k}\vec{d}_3} + e^{i\vec{k}\vec{d}_4}. \quad (\text{A6d})$$

The \vec{d}_j are the vectors connecting atom 1 to atom 2 in the unit cell and are given by $d_1 = \frac{a}{4}[111]$, $d_2 = \frac{a}{4}[1\bar{1}\bar{1}]$, $d_3 = \frac{a}{4}[\bar{1}1\bar{1}]$, and $d_4 = \frac{a}{4}[\bar{1}\bar{1}1]$, where a is the lattice constant.

While short-range elastic forces are described within the valence force field model, in crystal with an ionic contribution to the bonding, Coulomb interaction must also be included in the dynamical matrix. The long-range nature of the Coulomb interaction complicates the problem considerably. Using a pair-wise point charge model of the Coulomb interaction, the Coulomb dynamical matrix is given by³⁷:

$$D_{\alpha\alpha'}^c(\kappa, \kappa' | \vec{k}) = -\frac{q_\kappa q_{\kappa'}}{m_\kappa} \sum_{\kappa''} \phi_{\alpha\alpha'}(\kappa\kappa'' | 0) + \frac{1}{\sqrt{m_\kappa m_{\kappa'}}} \phi_{\alpha\alpha'}(\kappa\kappa' | \vec{k}) \quad (\text{A7})$$

where

$$\begin{aligned} \phi_{\alpha\alpha'}(\kappa, \kappa' | \vec{k}) = & -\frac{q_\kappa q_{\kappa'}}{4\pi\epsilon_0} P^{3/2} \\ & \times \sum_{l'} H_{\alpha\alpha'} \left(\sqrt{P}(\vec{x}(l, \kappa) - \vec{x}(l', \kappa')) \right) e^{i\vec{k}(\vec{x}(l, \kappa) - \vec{x}(l', \kappa'))} \\ & + \frac{q_\kappa q_{\kappa'}}{v_0\epsilon_0} \sum_G \frac{(\vec{G} + \vec{k})_\alpha (\vec{G} + \vec{k})_{\alpha'}}{|\vec{G} + \vec{k}|^2} \exp\left(-\frac{|\vec{G} + \vec{k}|^2}{4P}\right) \\ & \exp\left(i\vec{G}(\vec{x}(\kappa) - \vec{x}(\kappa'))\right). \end{aligned} \quad (\text{A8})$$

In the above equation l and κ label the unit cell and basis atoms, α refers to the cartesian component, q_κ is the effective charge, $\vec{x}(\kappa, l) = \vec{x}(\kappa) + \vec{x}(l)$ is the position vector of the κ^{th} atom in the l^{th} unit cell, \vec{G} are the reciprocal lattice vectors, v_0 is the unit cell volume, ϵ_0 is the permittivity constant, and P is a (numerically determined) measure of the Gaussian charge distribution used in the Ewald summation. $H_{\alpha, \alpha'}(y)$ is given by the integro-differential expression

$$H_{\alpha, \alpha'}(y) = \frac{2}{\sqrt{\pi}} \frac{\partial}{\partial y_\alpha} \frac{\partial}{\partial y_{\alpha'}} \left(\frac{1}{y} \int_y^\infty \exp(-x^2) dx \right). \quad (\text{A9})$$

The full dynamical matrix is given by the sum of the Coulomb and elastic contributions

$$D(\vec{k}) = D^c(\vec{k}) + D^e(\vec{k}). \quad (\text{A10})$$

In the present problem we are interested in calculating the change in the vibrational free energy of the crystal lattice due to the creation of a defect. This is done using the Green's function, which is most conveniently calculated in terms of the density of states of the phonon system. For the ideal crystal without a defect, a Brillouin zone integration is done to calculate the phonon density-of-states matrix, Θ , from which the Green's function can be calculated via

$$\begin{aligned} G^0(\omega^2) = & \int_{\omega_{\text{min}}^2}^{\omega_{\text{max}}^2} \frac{\Theta(\omega'^2) - \Theta(\omega^2)}{\omega'^2 - \omega^2 - i\eta} d\omega'^2 \\ & + \Theta(\omega^2) \ln \left(\frac{\omega^2 - \omega_{\text{min}}^2 - i\eta}{\omega^2 - \omega_{\text{max}}^2 - i\eta} \right) \end{aligned} \quad (\text{A11})$$

where the singularity in the integral has been explicitly removed. The change in the total density of states when a defect is introduced into the crystal can be deduced from Dyson's equation to obtain

$$\Delta\Theta(\omega^2) = \frac{1}{\pi} \text{Im} \frac{\partial}{\partial \omega^2} \ln (\det(1 - G^0(\omega^2)V)) \quad (\text{A12})$$

where V is the perturbation potential. In the present case we use a strictly site-diagonal perturbation potential corresponding to the mass change due to the introduction of an isolated defect.

The partition function for the phonon system in the zincblende lattice is given by

$$Z = \prod_i \left(\frac{\exp\left(\frac{-\hbar\omega_i}{2k_B T}\right)}{1 - \exp\left(\frac{-\hbar\omega_i}{k_B T}\right)} \right) \quad (\text{A13})$$

where ω_i are the normal modes of the system. The total vibrational entropy of the system is obtained from $S_{\text{total}}^{\text{vib}} = \frac{\partial}{\partial T}(k_B T \ln Z)$, which gives

$$S_{\text{total}}^{\text{vib}} = \sum_i \left(k_B \ln \left(\frac{1}{2} \sinh^{-1} \left(\frac{\hbar\omega_i}{2k_B T} \right) \right) + \frac{\hbar\omega_i}{2T} \coth \left(\frac{\hbar\omega_i}{2k_B T} \right) \right). \quad (\text{A14})$$

We convert the sum to an integral by the replacement

$$\sum_i \rightarrow \int_0^\infty \rho(\omega) d\omega = \int_0^\infty 2\rho(\omega^2) \omega d\omega \quad (\text{A15})$$

where $\rho(\omega^2) = \text{Tr} \Theta(\omega^2)$. We are interested in the change in the vibrational entropy upon formation of a defect, in which case we replace ρ by $\Delta\rho$ to obtain

$$S^{\text{vib}} = 2k_B \int_0^\infty \Delta\rho(\omega^2) \left(\frac{\hbar\omega}{2k_B T} \coth \left(\frac{\hbar\omega}{k_B T} \right) - \ln \left(2 \sinh \left(\frac{\hbar\omega}{2k_B T} \right) \right) \right) \omega d\omega. \quad (\text{A16})$$

Similarly for the vibrational energy, we use the relationship $U^{\text{vib}} = -\frac{\partial}{\partial(1/k_B T)} \ln Z$ to obtain

$$U^{\text{vib}} = 2 \int_0^\infty \Delta\rho(\omega^2) \left(\frac{\hbar\omega}{2} \coth \left(\frac{\hbar\omega}{2k_B T} \right) \right) \omega d\omega, \quad (\text{A17})$$

with the change in the vibrational free energy $F^{\text{vib}} = U^{\text{vib}} - TS^{\text{vib}}$.

While the calculation of the vibrational terms in this paper was done using the general expressions above, it is interesting to examine the expression for the free energy in the high temperature limit, that is appropriate for high growth and processing temperatures, and to examine the explicit temperature dependence of this term. In the high temperature limit $\hbar\omega_{\text{max}} \ll k_B T$ and F^{vib} reduces to

$$F^{\text{vib}} \approx 2k_B T \int_0^\infty \ln \left(\frac{\hbar\omega}{k_B T} \right) \rho(\omega) \omega d\omega. \quad (\text{A18})$$

This integral can be shown to be equal to

$$F^{\text{vib}} \approx k_B T n_m \ln \left(\frac{\hbar\bar{\omega}}{k_B T} \right) \quad (\text{A19})$$

where n_m is the number of phonon modes created or destroyed in the defect reaction of interest, and $\bar{\omega}$ is an appropriately weighted frequency. What enters the calculation of the defect concentrations is $\exp(-F^{\text{vib}}/k_B T)$ which reduces to

$$\exp \left(\frac{F^{\text{vib}}}{k_B T} \right) \approx \left(\frac{k_B T}{\hbar\bar{\omega}} \right)^{n_m} = C T^{n_m} \quad (\text{A20})$$

in the high temperature limit. For the defect reactions in Table I we obtain

$$\begin{array}{rcl}
& -3 & V_{Hg} \\
& 3 & V_{Te} \\
n_m = & 6 & Hg_{Te} \\
& -6 & Te_{Hg} \\
& +3 & Hg_I \\
& -3 & Te_I
\end{array}$$

(A21)

We will use this simple power-law dependence of Eq. (A20) to extract a simple power-law temperature dependence of the reaction constants.

- ¹ H. R. Vydyanath, J. Electrochem. Soc. 128, 2609 (1981).
- ² D. A. Stevenson and M-F. S. Tang, J. Vac. Sci. Technol. B 9, 1615 (1991), and references therein.
- ³ S. M. Johnson, D. R. Rhiger, J. P. Rosbeck, J. M. Peterson, S. M. Taylor, and M. E. Boyd, J. Vac. Sci. Technol. B 10, 1499 (1992).
- ⁴ S. H. Shin, J. M. Arias, D. D. Edwall, M. Sandian, J. G. Pasko, and R. E. DeWames, J. Vac. Sci. Technol. B 10, 1492 (1992).
- ⁵ R. S. List, J. Electron. Mater. 22, 1017 (1993).
- ⁶ H. R. Vydyanath, J. Appl. Phys. 65, 3080 (1989).
- ⁷ M. C. Chen, S. G. Parker, and D. F. Weirauch, J. Appl. Phys. 58, 3150 (1985).
- ⁸ R. Sporken, M. D. Lange, S. Sivanathan, and J. P. Faurie, Appl. Phys. Lett. 59, 81 (1991).
- ⁹ G. A. Baraff and M. Schlüter, Phys. Rev. Lett. 55, 1327 (1985); Phys. Rev. B 30, 1853 (1984); G. A. Baraff, E. O. Kane and M. Schlüter, *ibid.* 21, 5662 (1980).
- ¹⁰ D. B. Laks, C. G. Van de Walle, G. F. Newmark, and S. T. Pantelides, Phys. Rev. Lett. 66, 648 (1991); D. B. Laks, C.G. Van de Walle, G. F. Newmark, P.E. Blöchel, and S. T. Pantelides, Phys. Rev. B 45, 10965 (1992).
- ¹¹ J. Bernholc, N. O. Lipari, and S. T. Pantelides, Phys. Rev. B 21, 3545 (1980); J. Bernholc, and S. T. Pantelides, *ibid.* 18, 1780 (1978); J. Bernholc, N. O. Lipari, and S. T. Pantelides, Phys. Rev. Lett. 41, 895 (1978).
- ¹² S. B. Zhang and D. J. Chadi, Phys. Rev. Lett. 64, 1789 (1990).
- ¹³ M. A. Berding, M. van Schilfgaarde, A. T. Paxton, and A. Sher, J. Vac. Sci. Technol. A 8, 1103 (1990).
- ¹⁴ M. A. Berding, M. van Schilfgaarde, and A. Sher, J. Vac. Sci. Technol. B 10, 1471 (1992).
- ¹⁵ M. A. Berding, A. Sher, and A.-B. Chen, J. Appl. Phys. 68, 5064 (1990); J. Vac. Sci. Technol. A 5, 3009 (1987).
- ¹⁶ J. T. Schick and C. G. Morgan-Pond, J. Vac. Sci. Technol. A 8, 1108 (1990); C. G. Morgan-Pond and R. Raghavan, Phys. Rev. B 31, 6616 (1985).
- ¹⁷ Preliminary results of this work have been published in M. A. Berding, M. van Schilfgaarde, and A. Sher, J. Electron. Mater. 22, 1005 (1993).
- ¹⁸ O. K. Andersen, O. Jepsen, and D. Glotzel, *Highlights of condensed matter theory*, F. Bassani et al., Amsterdam, North Holland (1985) p. 59.
- ¹⁹ D. Langreth and D. Mehl, Phys. Rev. B 28, 1809 (1983).
- ²⁰ M. van Schilfgaarde, A.T. Paxton, M. A. Berding, and M. Methfessel (in preparation).
- ²¹ F. A. Kröger, *The Chemistry of Imperfect Crystals* (J. Wiley & Sons, Inc., New York, 1964).
- ²² F. A. Kröger and H. J. Vink, in *Solid State Physics Vol. 3*, edited by F. Seitz and D. Turnbull (Academic Press, New York 1956), p. 307.
- ²³ S. Krishnamurthy and A. Sher, presented at *The 1993 U.S. Workshop on the Physics and Chemistry of Mercury Cadmium Telluride and other IR Materials*, October 19-21, Seattle, Washington.
- ²⁴ M. Methfessel and M van Schilfgaarde (unpublished).
- ²⁵ U. von Barth and L. Hedin, J. Phys. C5, 1629 (1972).
- ²⁶ M. Methfessel, Phys. Rev. B38, 1537 (1988).
- ²⁷ R. Jones and A. Sayyesh, J. Phys. C, L653 (1986).
- ²⁸ J. P. Hirth and J. Lothe, *Theory of Dislocations*, (J. Wiley & Sons, Inc., New York, 1982) pg. 49.
- ²⁹ E. R. Weber, H. Ennen, U. Kaufmann, J. Windscheif, J. Schneider, and T. Wosinski, J. Appl. Phys. 53, 6140 (1982).
- ³⁰ C. G. van der Waal, P. J. H. Denteneer, Y. Bar-Yam, and S. T. Pantelides, Phys. Rev. B 39, 10791 (1989).
- ³¹ D. E. Cooper and W. A. Harrison, J. Vac. Sci. Technol. A 8, 1112 (1990).
- ³² For a general discussion of the calculation of state degeneracy in semiconductors, see E. A. Guggenheim, Proc. Phys. Soc. A, 66, 121 (1953), and references therein.
- ³³ G. L. Hansen and J. L. Schmit, J. Appl. Phys. 54, 1639 (1983).

- ³⁴ G. L. Hansen, J. L. Schmit and T. N. Casselman, *J. Appl. Phys.* **53** 7099, (1982).
³⁵ There has been a recent attempt to predict the intrinsic carrier concentrations at temperatures up to 600°C by M. Wienecke, M. Schenk, and H. Berger, *Semicond. Sci. Technol.* **8**, 299 (1993), although their analysis is suspect because of the temperature dependencies they have assumed for the high-temperature mobility.
³⁶ P. N. Keating, *Phys. Rev.* **145**, 637 (1966).
³⁷ A. A. Maradudin, E. W. Montroll, G. H. Weiss, and I. P. Ipatova, in *Solid State Physics Supp. 3*, edited by H. Ehrenreich, F. Seitz and D. Turnbull (Academic Press, New York 1971), p. 1.
³⁸ W. A. Harrison, *Electronic Structure and the Properties of Solids* (W. H. Freeman and Company, San Francisco, 1980).
³⁹ J. L. Meléndez and C. R. Helms, presented at *The 1993 U.S. Workshop on the Physics and Chemistry of Mercury Cadmium Telluride and other IR Materials*, October 19-21, Seattle, Washington.
⁴⁰ H. F. Schaake and J. H. Tregilgas, *J. Electron. Mater.* **12**, 931 (1983).

FIG. 1. Calculated phonon dispersion curve for HgTe

FIG. 2. Defect concentrations at annealing temperature for material annealed at (a) 250°C, (b) 500°C, and (c) 655°C.

FIG. 3. Defect concentrations for 500°C anneal after quench cooling to 77 K.

FIG. 4. Hole concentrations at 77 K for material equilibrated at various high-temperature annealing conditions. Experimental results taken from Ref. (1).

FIG. 5. Hole concentrations at 77 K for material equilibrated at various high-temperature annealing conditions, calculated with the electronic formation energy for the mercury vacancy increased by 10% and a rigid upward shift of the hole concentrations by a factor of 2.2. This figure is meant to demonstrate the sensitivity of our results to small changes in our calculated parameters. As discussed in the text, similar qualitative changes in our results can be seen by modifying the intrinsic reaction constant.

FIG. 6. Defect concentrations for material annealed along the mercury-rich side of the stability region at (a) the annealing temperature and (b) after quenching to 77 K.

TABLE I. Defect reactions considered for compound AC. Notation is as follows: The primary symbol refers to the species, the subscript refers to the site that the species occupies, with no subscript indicating that the species is occupying its usual lattice site. V corresponds to a vacancy, I an interstitial, R some external reference state, and X a generic defect. Two types of interstitials are considered, both occupying tetrahedral sites, the first surrounded by four cation nearest neighbors, I_C , the second surrounded by four anion nearest neighbors, I_A . Following the notation of Kröger,²¹ an \times superscript corresponds to a neutral species, a prime to a negatively charged species, a bullet to a positively charged species, and e' and h° are an electron and hole, respectively.

AC	\longrightarrow	$V_A^\times C + A_R$	(1)
A_R	\longrightarrow	AV_C^\times	(2)
$2A_R$	\longrightarrow	AA_C^\times	(3)
$2AC$	\longrightarrow	$C_A^\times C + 2A_R$	(4)
A_R	\longrightarrow	$A_{I_A}^\times$	(5)
A_R	\longrightarrow	$A_{I_C}^\times$	(5')
AC	\longrightarrow	$C_{I_A}^\times + A_R$	(6)
AC	\longrightarrow	$C_{I_C}^\times + A_R$	(6')
X^\times	\longrightarrow	$X_{II}^\times + sh^\circ$	(7)
X^\times	\longrightarrow	$X^{so} + ze'$	(8)
$e' + h^\circ$	\longrightarrow	0	(9)

TABLE II. Bulk cohesive energies with and without the gradient corrections (GC) to the local density (LD), and comparison with experiment.

Compound	LD	Cohesive energy (eV/bond)		Experiment
		GC		
Si	2.58	2.31		2.32
Ge	2.22	1.88		1.94
AlP	2.35	2.05		2.13
AlAs	2.17	1.85		1.89
AlSb	1.91	1.61		1.76
GaP	2.08	1.76		1.78
GaAs	1.91	1.56		1.63
1 GaSb	1.70	1.36		1.48
InP	1.89	1.56		1.74
InAs	1.77	1.42		1.55
InSb	1.60	1.26		1.40
ZnS	1.82	1.53		1.59
ZnSe	1.64	1.35		1.29
ZnTe	1.43	1.15		1.20
CdTe	1.33	1.04		1.10
HgS	1.29	0.94		1.02
HgSe	1.19	0.84		0.85
HgTe	1.09	0.76		0.81

TABLE III. Neutral native defect formation energies for HgTe corresponding to reactions in Table I, where A is mercury, B is tellurium, and the free atom is used as the reference state A_R . Local-density (LD) calculations were done using a 16-atom supercell, unless otherwise noted. Gradient correction (GC) energies are discussed in the text. The most important ionization states of the native point defects are also given.

Defect	Energy (eV)				Ionization State
	LD	Relaxation ^a	GC	Total	
V_{Hg}	2.83	-0.05	-0.69	2.09	double acceptor ^a
V_{Te}	0.99	-0.01	0.49	1.47	shallow donor
Hg_{Te}	-1.00	0	1.46	0.46	deep acceptor
Te_{Hg}	4.85	-0.19	-1.54	3.12	shallow donor
Hg_{Hg}	0.75	-0.24	0.70	1.21	shallow donor
Hg_{Te}	0.81	-0.31	0.62	1.12	shallow donor
Te_{Hg}	4.78	-0.57	-0.83	3.38	shallow donor
Te_{Te}	5.17	-0.84	-0.96	3.37	shallow donor

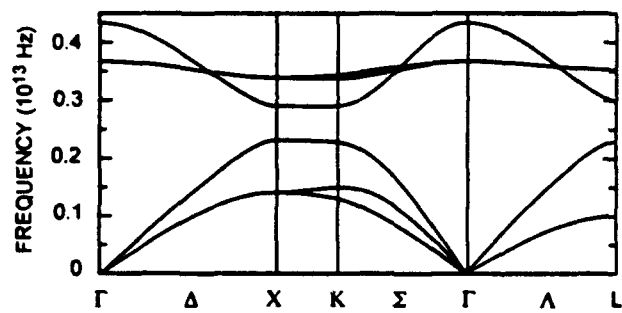
^a Assumed to be a negative-U center

TABLE IV. Entropy (S^{vb}) and energy (U^{vb}) contributions to the vibrational free energy in HgTe at 500°C, for the defect reactions listed in Table I.

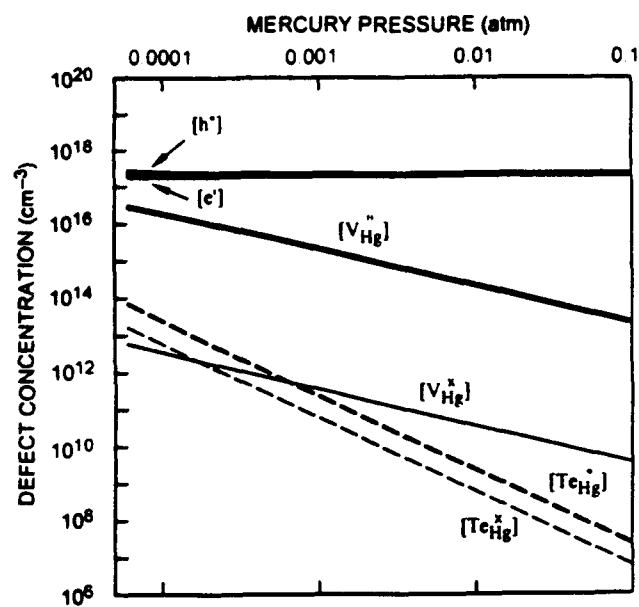
Defect	$S^{vb}(k_B)$	$U^{vb}(eV)$
V_{Hg}	-8.9	-0.20
V_{Te}	9.7	0.19
Hg_{Te}	18.7	0.39
Te_{Hg}	-18.7	-0.39
Hg_I	9.5	0.20
Te_I	-9.5	-0.20

TABLE V. Reaction constants for neutral defects in $Hg_{0.8}Cd_{0.2}Te$ corresponding to the defect reactions in Table I. The vibrational contribution is calculated at 500°C, and fit to the high-temperature power-law dependence [Eq. A19] so as to show the explicit temperature dependence. All calculations in the paper were done using reaction constants with the more exact expression for the vibrational free energies.

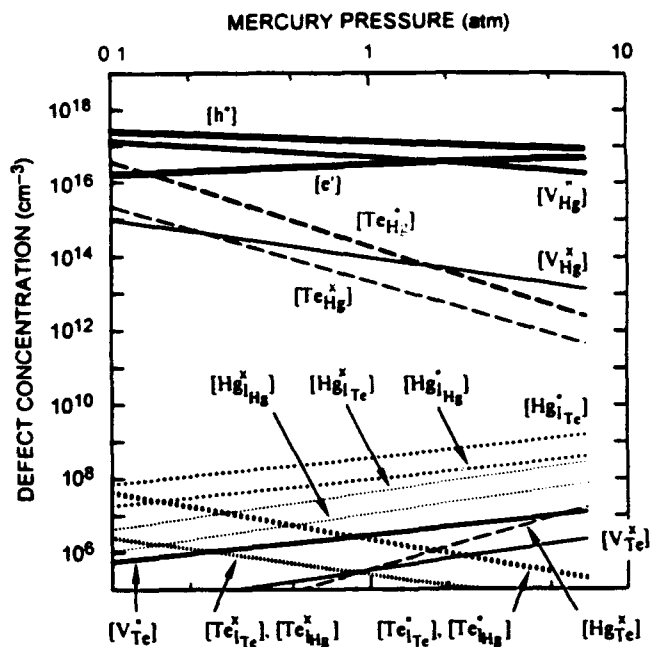
Defect	Reaction Constant
V_{Hg}^x	$K_{V_{Hg}^x} = [V_{Hg}^x] = 1.14 \times 10^{30} T^{-\frac{1}{2}} P_{Hg}^{-1} \exp(-\frac{2.09}{k_B T})$
V_{Te}^x	$K_{V_{Te}^x} = [V_{Te}^x] = 4.55 \times 10^{14} T^{\frac{1}{2}} P_{Hg} \exp(-\frac{1.97}{k_B T})$
Hg_{Te}^x	$K_{Hg_{Te}^x} = [Hg_{Te}^x] = 4.47 \times 10^6 T^1 P_{Hg}^2 \exp(-\frac{0.46}{k_B T})$
Te_{Hg}^x	$K_{Te_{Hg}^x} = [Te_{Hg}^x] = 3.80 \times 10^{37} T^{-1} P_{Hg}^{-2} \exp(-\frac{3.12}{k_B T})$
$Hg_{I_{Hg}}^x$	$K_{Hg_{I_{Hg}}^x} = [Hg_{I_{Hg}}^x] = 3.03 \times 10^{14} T^{\frac{1}{2}} P_{Hg} \exp(-\frac{1.21}{k_B T})$
$Hg_{I_{Te}}^x$	$K_{Hg_{I_{Te}}^x} = [Hg_{I_{Te}}^x] = 3.03 \times 10^{14} T^{\frac{1}{2}} P_{Hg} \exp(-\frac{1.12}{k_B T})$
$Te_{I_{Hg}}^x$	$K_{Te_{I_{Hg}}^x} = [Te_{I_{Hg}}^x] = 7.23 \times 10^{29} T^{-\frac{1}{2}} P_{Hg}^{-1} \exp(-\frac{3.38}{k_B T})$
$Te_{I_{Te}}^x$	$K_{Te_{I_{Te}}^x} = [Te_{I_{Te}}^x] = 7.23 \times 10^{29} T^{-\frac{1}{2}} P_{Hg}^{-1} \exp(-\frac{3.37}{k_B T})$



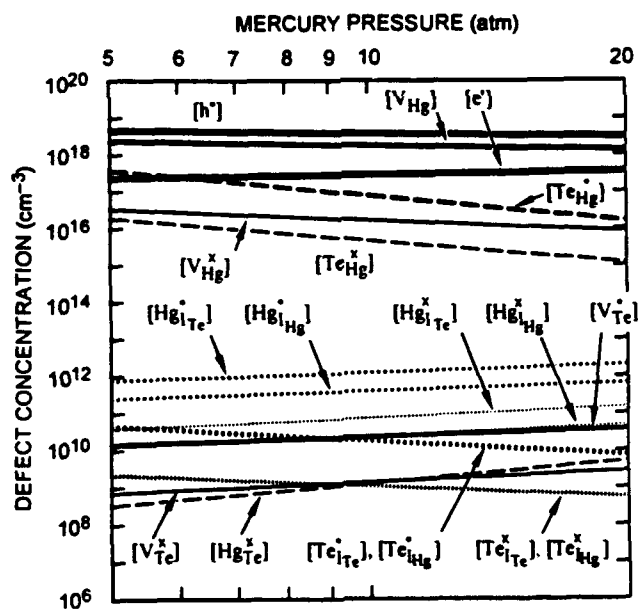
M. Berding
Figure 1



(a)

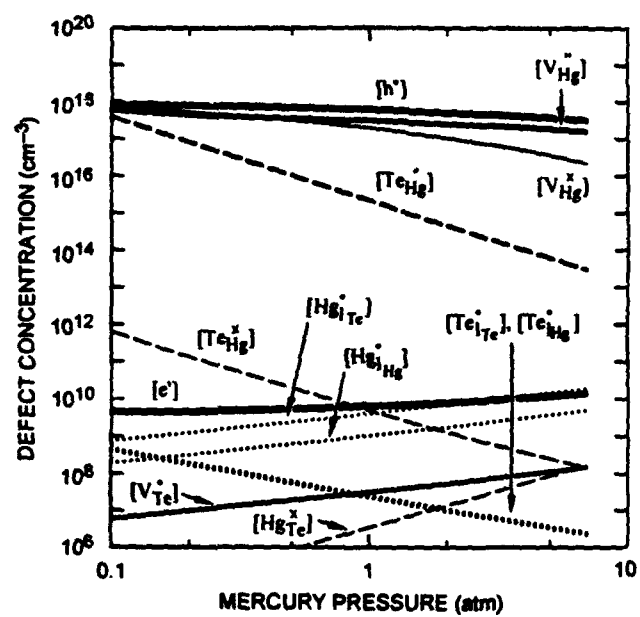


(b)

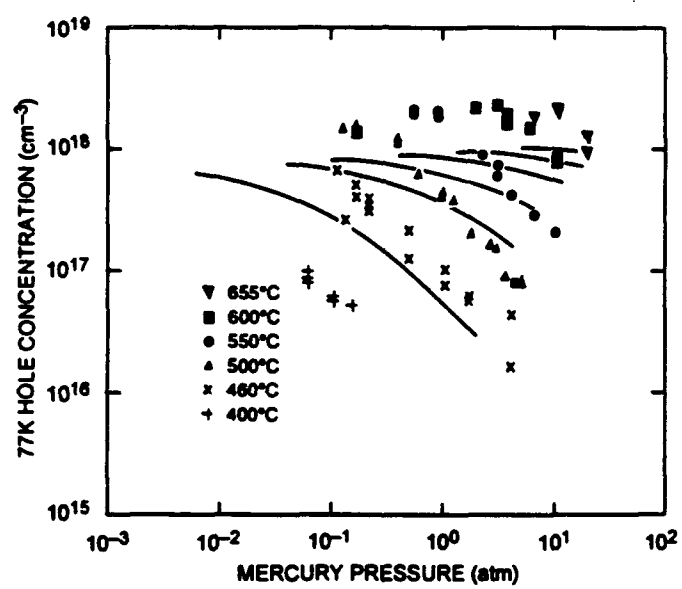


(c)

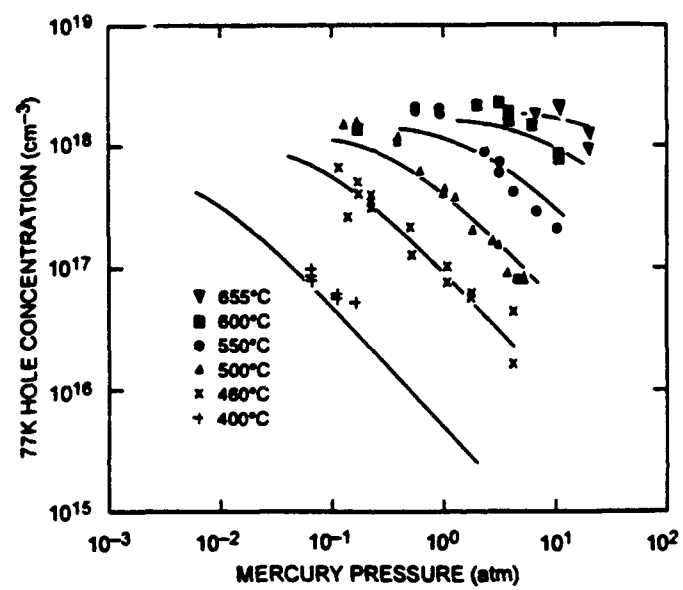
M. Berding
Figure 2



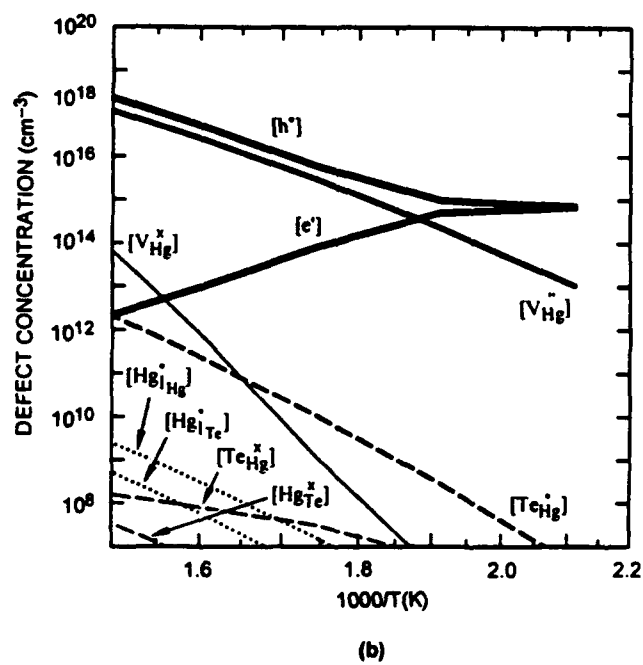
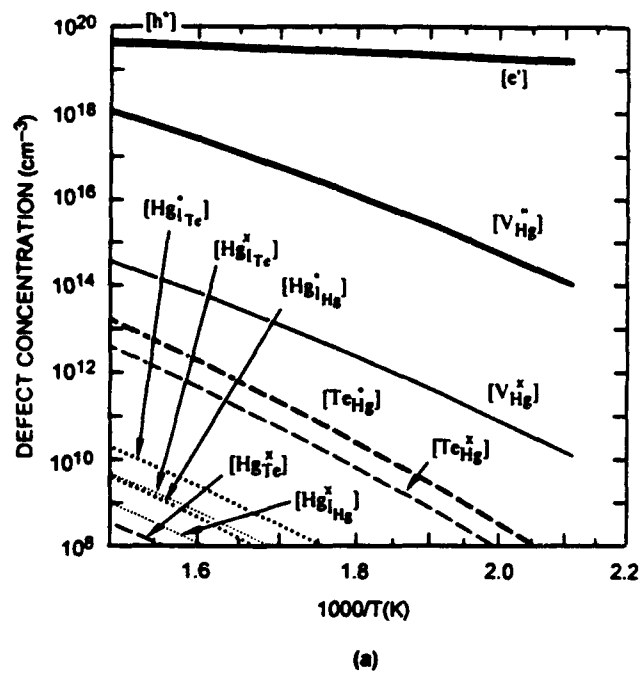
M. Berding
Figure 3



M. Berding
Figure 4



M. Berding
Figure 5



M. Berding
Figure 6

APPENDIX B

Summary of correspondence with Dr. M. Haase and Dr. Diego Olego



Dr. Marcy Berding
Physical Electronics Lab.
SRI International, 410-33
Menlo Park, CA 94025

February 2, 1994

Dr. Anis Husain
ARPA
3701 N. Fairfax Drive
Arlington, VA 22203

Dear Dr. Husain

In response to your suggestions at the meeting with Arden Sher last month, we have spoken to both Dr. Diego Olego at Philips Lab and Dr. Michael Haase at 3M about their work in ZnSe-based laser technology. These conversations were extremely useful and both groups were interested in having us pursue solutions to a number of their problems.

As a result of these conversations, we were able to identify several areas in which our capabilities could be applied to current problems in ZnSe-based laser technology. These areas are summarized below:

DOPING

Doping is still an area of great interest and remains a performance limiter. Although some success has been achieved with nitrogen, what is limiting the achievable p-type doping levels is still a mystery that both groups are anxious to have solved. Some curious effects have also been seen, such as a reduction in the p-type conductivity directly under ZnTe contacts. While both groups were less optimistic about the prospects of achieving high levels of p-doping with phosphorus or arsenic, they both thought it should be an area of continued research.

We are currently working on the issue of doping under our ARPA sponsorship. The problem of native defects is central to answering the compensation question. We will also be looking at solubility limits of various dopants. Our proposed work on dopants was of interest to both experimental groups, because it will provide guidance about which dopant is most likely to succeed, and an opportunity for cost reduction. Unfortunately, at our current rate of funding, it will be over a year until we finish these calculations.

SRI International

333 Ravenswood Ave. • Menlo Park, CA 94025 • (415) 326-6200 • TWX: 910-373-2046 • Telex: 334486 • Facsimile: (415) 326-5512

The efficiency of dopants is often related to complex formation. Both groups find there is more nitrogen incorporation than there are active acceptors. In other materials this is often the result of complex formation, either between impurity atoms or between an impurity and a native point defect. We are currently calculating complex formation energies in HgCdTe and heavily arsenic-doped silicon. Our current program on ZnSe does not include work on complexes.

There a number of extensions we can make to our work to study the doping near interfaces such as ZnSe/ZnTe; for example, once we have completed our current work, it would be straightforward to extend our calculations to include band bending at the interface, and to predict the resulting modifications in the equilibrium doping efficiency. We can also explore nonequilibrium impurity and defect densities that may result when growth occurs at temperatures below which diffusion of the relevant species stops. We also have tools in hand to consider modifications to the bulk doping that results from alloying ZnSe with other elements such as sulfur, cadmium, and tellurium.

DARK LINE DEFECTS

This was the area of most interest to both groups, since dark line defects are limiting device lifetimes, preventing products from being brought to market. While the dark line defects appear to be related to dislocations and perhaps native point defects, the full relationship is still not understood. As devices degrade, the dark areas grow, but it is not obvious whether it is dislocation multiplication or modifications to the defect atmosphere around existing dislocations that result in the device failure. There also seems to be a correlation of device failure with stacking faults originating at the ZnSe/GaAs interface, and removal of these faults is of critical importance. While the propagation of dislocations through the active QW structure is correlated with failure of the devices, the means by which the devices fail is still not clear; that is, do the dislocations short the junction, or do they just act as recombination sites.

The area of the impact of dislocations on device performance is an area we have been just recently working in the context of HgCdTe double-layer heterojunction devices. There we examined the impact of both the dislocation strain field (and the resulting piezoelectric charge) and core charges. This theory can be easily extended to ZnSe-based laser structures. In addition, this work can be extended to examine the nature of the material in the vicinity of the dislocation, for example native defect and impurity populations, and their correlation with the observed growth in the area of dark line defects. While the properties of stacking faults - for example, their energy - can be examined using our tools, most of the technological concern is in elimination of the stacking faults, which is closely coupled to the MBE growth process, discussed further below.

BAND STRUCTURE PROPERTIES

While many ZnSe-based alloys are used in current ZnSe-based lasers, very little is known about the band offsets among the constituents. We were told that knowledge of these offsets would greatly help in device analysis and design. In addition, more information on the band gap variation with composition in alloys such as ZnSSe, ZnCdSe, ZnSeTe, and ZnMgSSE would be extremely useful. The area of valence-band offsets is also of interest for the new alloy system, ZnSeTe, being explored for its ease of p-type doping and ability to make ohmic contacts

Once again, this is an area in which our alloy theory group has had extensive experience. We have calculated the band structure of most of the group IV, III-V, and II-VI compounds and many of their alloys. Our results have been in quantitative agreement with experiment. We have also applied these techniques to new alloy systems, such as HgZnTe, and our results were later substantiated by experiments. Accurate calculations of band offsets among the II-VI compounds and their alloys are also possible using a combination of our techniques: the first-principles full-potential linearized muffin-tin orbital and the tight-binding-based coherent potential approximation (CPA) method.

MOLECULAR BEAM EPITAXY (MBE)

The major successes to date in the ZnSe-based laser technology have been with materials grown by MBE and doped with nitrogen. While great progress has been made, a number of issues relating to growth must still be addressed. One of these relates to the failure mechanism and its relationship to stacking faults at the III-V/ II-VI interface. While MBE growth parameters have been optimized to eliminate the formation of interfacial phases such as Ga_2Se_3 , elimination of stacking faults still remains an issue. Issues of doping also closely relate to the growth process, as is well known from the need to use a plasma source for nitrogen cracking to obtain the current nitrogen doping levels.

The current limitation in the p-doping levels achievable may be related to the growth itself, rather than a fundamental solubility limitation or native defect. In our past work we have demonstrated that in some wide-gap ionic materials, atoms on the surface have a mutually repulsive interaction, resulting in ordered arrays of surface atoms and vacancies. The occurrence of this ordering depends on the surface orientation, substrate temperature, effective atomic fluxes and surface stabilization, and surface coverage. Substantial ordering may occur for only the cation or anion layer. When present, this ordering will modify the nature of nonisoelectronic impurity and alloy constituent incorporation into the layer. This theory predicts the observed ordering in MBE-grown GaAlAs, and is currently being experimentally tested for silicon impurity incorporation in GaAs.

PROPOSED TASK LIST

Based on our discussions with the experimental groups, very briefly outlined above, we have developed a task list for an extension of our current program on ZnSe. Following the task list is an estimate of the man-years required for its accomplishment. We have not provided a description of the methods we will employ in carrying out these tasks, nor references to our prior publications in the relevant fields. However, in all of the proposed tasks we have from moderate to extensive relevant previous work.

TASK 1

Devise means to improve p-doping in ZnSe-based materials, increasing dopant incorporation and efficiency.

1.1 Extend our current program to calculate the equilibrium solubility of isolated impurities for the most promising dopants in ZnSe, including nitrogen, phosphorus and arsenic. Determine if currently realized limits for active nitrogen incorporation are due to equilibrium solubility effects and, if not, what are those limits. Determine if any impurity looks more promising than nitrogen.

1.2 Calculate the density of defect pairs, including impurity-impurity and impurity-defect pairs, with the aim of determining if pairing is limiting the doping efficiency. The impurities to be considered depend on the predicted solubilities in Task 1.1.

1.3 Based on results from Tasks 1.1 and 1.2, devise a strategy to improve the doping levels obtainable in ZnSe-based materials.

1.4 Examine the nature of the ZnSe/ZnTe interface to seek an explanation for the reduced solubility of nitrogen there. Propose means by which to increase the local solubility.

1.5 Consider modifications to all of the above based on the fact that the material may be in quasi-equilibrium during and following the low-temperature MBE growth.

TASK 2

Develop means by which to increase the operational life of ZnSe-based LEDs and Lasers.

2.1 Extend our theory of dislocations and their impact on HgCdTe devices, to ZnSe-based laser structures. Determine the means by which dislocations impact device operation and correlate dislocation density with device efficiency.

2.2 Determine impurity and native defect atmospheres about dislocations due to both Coulomb and strain fields. Consider how these atmospheres change during the operational lifetime of devices, including effects of nonradiative-recombination-induced bond-breaking near the p-n junctions and thermal heating.

2.3 Based on the results of Task 4, examine mechanisms responsible for causing stacking faults in MBE growth at the ZnSe/GaAs interface, and devise strategies to eliminate them.

TASK 3

Provide parameters needed for design of present and future ZnSe-based Lasers.

3.1 Calculate the band structures of ZnSe and related alloys. Calculate the band-gap bowing as a function of alloy composition. These calculations will also provide the wave functions needed for other tasks listed below.

3.2 Predict the band offsets among the alloys and compounds relevant to the ZnSe-based laser technology, as specified by the experimental groups.

3.3 Calculate the nonradiative lifetimes for the relevant mechanisms of Auger, and Shockley-Read for impurities and native point defects present in significant concentrations.

TASK 4

Optimize MBE growth parameters for incorporation of active dopants and for minimization of structural defects.

4.1 Apply our current models of surfaces to ZnSe and related materials to predict the nature of the surfaces during MBE growth. Determine the nature of the impurity-host interactions on the surface and predict optimal parameters for active dopant incorporation.

4.2 Develop a full MBE growth simulator based on our current first-principles molecular dynamics methods. Apply the simulator to the problem of the GaAs/ZnSe-based material interface to predict the occurrence of stacking faults; optimize growth parameters to minimize stacking fault densities. Exercise the model in numerous other applications relevant to the growth of ZnSe-based laser devices.

Assuming a 3-year effort, we have estimated 1.25 man-years to accomplish Task 1, 0.75 man-year for Task 2, 0.5 man-year for Task 3, and 1.5 man-years for Task 4. While most of the work is devoted to the ZnSe-based systems, the development of an MBE simulator under Task 4 would be applicable to many other systems in addition to ZnSe.

Tasks 1 and 4 are especially computationally intensive, and will require the purchase of a workstation with about 128 MBytes of memory. We estimate this would cost approximately \$50,000.

Although neither Dr. Haase nor Dr. Olego informed us that our conversations were confidential, we hesitate to send them this letter because it contains information extracted from both conversations. However, we certainly will be comfortable if you choose to send copies of this letter along to them for feedback.

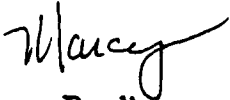
To Dr. Anis Husain

February 2, 1994

Page 6

We are very excited about getting a start on the tasks outlined above. We feel these tasks are in areas in which we can effectively collaborate with the experiment teams and make a substantial impact on the technology. We will call you in few weeks to obtain your feedback on this proposed program.

Sincerely,



Marcy Berding
Senior Research Physicist



Arden Sher
Associate Director,
Physical Electronics Laboratory

MB/mb

P. S. We have just receive a letter from Dr. Atsuko Ebina of Tohoku University who is working on ZnSeSe and ZnSeTe and who has just obtained some very interesting results on the band structure of these alloys as a function of alloy composition. A copy of her letter and a couple of the numerous figures she sent us are attached. She will be just down the road at Stanford University this summer working with Professor Spicer and would like to collaborate with us. Because we have done extensive work in the theory of alloy ordering and phase transitions in the semiconductor alloys, we know that we could have an effective and fruitful collaboration with her. The results of such an effort would greatly benefit the U.S. experimental groups. As such, we would like to include an additional task to collaborate with Dr. Ebina as well as the U.S. experimental groups and to apply our alloy theory of the phase transition to the ZnSSe and ZnSeTe systems. We expect this would require of the order of 0.5 manyear.